Astronomy & Astrophysics

ESO-Hα 574 and Par-Lup 3-4 jets: Exploring the spectral, kinematical, and physical properties[⋆,⋆⋆]

E. T. Whelan[1], R. Bonito[2,3], S. Antoniucci[4], J. M. Alcalá[5], T. Giannini[4], B. Nisini[4], F. Bacciotti[6], L. Podio[6,7], B. Stelzer[3], and F. Comerón[8]

[1] Institut für Astronomie und Astrophysik, Kepler Center for Astro and Particle Physics, Eberhard Karls Universität, 72076 Tübingen, Germany
e-mail: emma.whelan@astro.uni-tuebingen.de
[2] Università di Palermo, P.zza del Parlamento 1, 90134 Palermo, Italy
[3] INAF – Osservatorio Astronomico di Palermo, Piazza del Parlamento 1, 90134 Palermo, Italy
[4] INAF – Osservatorio Astronomico di Roma, via Frascati 33, 00040 Monte Porzio, Italy
[5] INAF – Osservatorio Astronomico di Capodimonte, via Moiariello, 16, 80131 Napoli, Italy
[6] INAF – Osservatorio Astrofisico di Arcetri, Largo E. Fermi 5, 50125 Firenze, Italy
[7] UJF-Grenoble 1/CNRS-INSU, Institut de Planétologie et d'Astrophysique de Grenoble (IPAG) UMR 5274, 38041 Grenoble, France
[8] ESO, Alonso de Córdova 3107, Castilla 19001, Santiago 19, Chile

ABSTRACT

In this paper a comprehensive analysis of VLT/X-Shooter observations of two jet systems, namely ESO-Hα 574 a K8 classical T Tauri star and Par-Lup 3-4 a very low mass (0.13 $M_\odot$) M5 star, is presented. Both stars are known to have near-edge on accretion disks. A summary of these first X-shooter observations of jets was given in a 2011 letter. The new results outlined here include flux tables of identified emission lines, information on the morphology, kinematics and physical conditions of both jets and, updated estimates of $\dot{M}_{\rm out}/\dot{M}_{\rm acc}$. Asymmetries in the ESO-Hα 574 flow are investigated while the Par-Lup 3-4 jet is much more symmetric. The density, temperature, and therefore origin of the gas traced by the Balmer lines are investigated from the Balmer decrements and results suggest an origin in a jet for ESO-Hα 574 while for Par-Lup 3-4 the temperature and density are consistent with an accretion flow. $\dot{M}_{\rm acc}$ is estimated from the luminosity of various accretion tracers. For both targets, new luminosity relationships and a re-evaluation of the effect of reddening and grey extinction (due to the edge-on disks) allows for substantial improvements on previous estimates of $\dot{M}_{\rm acc}$. It is found that $\log(\dot{M}_{\rm acc}) = -9.15 \pm 0.45$ $M_\odot$ yr^{-1} and -9.30 ± 0.27 $M_\odot$ yr^{-1} for ESO-Hα 574 and Par-Lup 3-4 respectively. Additionally, the physical conditions in the jets (electron density, electron temperature, and ionisation) are probed using various line ratios and compared with previous determinations from iron lines. The results are combined with the luminosity of the [SII]λ6731 line to derive $\dot{M}_{\rm out}$ through a calculation of the gas emissivity based on a 5-level atom model. As this method for deriving $\dot{M}_{\rm out}$ comes from an exact calculation based on the jet parameters (measured directly from the spectra) rather than as was done previously from an approximate formula based on the value of the critical density at an assumed unknown temperature, values of $\dot{M}_{\rm out}$ are far more accurate. Overall the accuracy of earlier measurements of $\dot{M}_{\rm out}/\dot{M}_{\rm acc}$ is refined and $\dot{M}_{\rm out}/\dot{M}_{\rm acc} = 0.5$ (+1.0)(−0.2) and 0.3 (+0.6)(−0.1) for the ESO-Hα 574 red and blue jets, respectively, and 0.05 (+0.10)(−0.02) for both the Par-Lup 3-4 red and blue jets. While the value for the total (two-sided) $\dot{M}_{\rm out}/\dot{M}_{\rm acc}$ in ESO-Hα 574 lies outside the range predicted by magneto-centrifugal jet launching models, the errors are large and the effects of veiling and scattering on extinction measurements, and therefore the estimate of $\dot{M}_{\rm acc}$, should also be considered. ESO-Hα 574 is an excellent case study for understanding the impact of an edge-on accretion disk on the observed stellar emission. The improvements in the derivation of $\dot{M}_{\rm out}/\dot{M}_{\rm acc}$ means that this ratio for Par-Lup 3-4 now lies within the range predicted by leading models, as compared to earlier measurements for very low mass stars. Par-Lup 3-4 is one of a small number of brown dwarfs and very low mass stars which launch jets. Therefore, this result is important in the context of understanding how $\dot{M}_{\rm out}/\dot{M}_{\rm acc}$ and, thus, jet launching mechanisms for the lowest mass jet driving sources, compare to the case of the well-studied low mass stars.

Key words. stars: formation – ISM: jets and outflows – accretion, accretion disks – line: identification

1. Introduction

The mass outflow phase is a key stage in the star formation process. Protostellar jets (fast, collimated outflows) are an important manifestation of the outflow phenomenon and it is generally

accepted that they are strongly connected with accretion (Cabrit 2007). The importance of these jets lies in the fact that they are the likely mechanism by which angular momentum is removed from the star-disk system (Coffey et al. 2004). While jets from low mass young stellar objects (YSOs) have been studied now for several decades, more recently it has been found that very low mass stars (VLMS) and brown dwarfs (BDs) also drive jets during their formation (Joergens et al. 2013). The jets of VLMSs and BDs have many similarities with jets of low mass YSOs. For example, they have been found to be collimated, episodic, and asymmetric (Whelan et al. 2009, 2012), they can

---

have multi-component velocity profiles (Whelan et al. 2009), and they are associated with a molecular counterpart (Monin et al. 2013). Therefore, it is possible that the mechanisms responsible for the launching and collimation of protostellar jets also operate down to substellar masses (Whelan et al. 2009).

Although a magneto-centrifugal jet launching model is favoured for the production of jets, the precise scenario is still debated (Ferreira 2013; Frank et al. 2014) and, thus observational constraints are currently needed. Protostellar jets are characterised by an abundance of shock excited emission lines and analysis of these emission regions, using both spectroscopy and imaging, offers a wealth of information pertinent to jet launching models. Of particular value are spectroscopic observations which simultaneously cover different wavelength regimes. Such observations allow outflow and accretion properties to be investigated from the same dataset and over a significant range in wavelength, leading, for example, to more accurate estimates of the ratio of mass outflow to accretion ($\dot{M}_{out}/\dot{M}_{acc}$). For instance, studies have shown that the optimum way to measure $\dot{M}_{acc}$ is by using several different accretion indicators, found in different wavelength regimes (Rigliaco et al. 2011, 2012). In this way any spread in $\dot{M}_{acc}$ due to different indicators probing different regimes of accretion or having varying wind/jet contributions can be overcome. Magneto-centrifugal jet launching models place an upper limit (per jet) of ~0.3 on $\dot{M}_{out}/\dot{M}_{acc}$ (Ferrreira et al. 2006; Cabrit 2009). Therefore it is important to measure this ratio not only in low mass YSOs but also in VLMSs and BDs. $\dot{M}_{out}/\dot{M}_{acc}$ has been constrained at 1% to 10% for T Tauri stars (class II low mass YSOs; TTSs; Hartigan et al. 1995; Melnikov et al. 2009; Agra-Amboage et al. 2009). Initial attempts at estimating $\dot{M}_{out}/\dot{M}_{acc}$ in VLMSs/BDs produced results which suggested that this ratio is higher in BDs than in TTSs and at most to be comparable (Comerón et al. 2003; Whelan et al. 2009). More recent studies of the VLMS ISO 143 and the BD FU Tau A, produced ratios which are more in line with studies of TTS (Joergens et al. 2012b; Stelzer et al. 2013). Thus much work is still needed to constrain $\dot{M}_{out}/\dot{M}_{acc}$ at the lowest masses. This work will involve overcoming various observational uncertainties which are outlined in the above papers and addressed as part of this work.

X-Shooter, one of the newest instruments on the European Southern Observatory's (ESO) Very Large Telescope (VLT), provides contemporaneous spectra in the ultraviolet (UVB), visible (VIS), and near-infrared (NIR) regimes, with a total coverage of ~300 nm to 2500 nm. With the aim of exploring the advantages of X-Shooter for the study of outflow and accretion activity in YSOs/BDs, we conducted in 2010 a pilot X-Shooter study of two YSOs. The targets were the classical T Tauri star (CTTS) ESO-Hα 574 and the VLMS Par-Lup 3-4 (see Sect. 2). As these were the first X-Shooter observations of YSO jets the initial results and spectra were published in a letter (Bacciotti et al. 2011). In addition, the numerous [Fe II] and [Fe III] detected lines have been discussed in Giannini et al. (2013), where the potential of UV-VIS-NIR Fe line diagnostics in deriving the jet physical parameters is demonstrated. The [Fe II] line analysis revealed that the ESO-Hα 574 jet is, on average, colder, less dense, and more ionised than the Par-Lup 3-4 jet. The physical conditions derived from the iron lines were also compared with shock models which pointed to the ESO-Hα 574 shock likely being faster and more energetic than the Par-Lup 3-4 shock. In Bacciotti et al. (2011), outflow and accretion tracers present in the spectra were examined, the effect of extinction by an edge-on disk was discussed, and first estimates of $\dot{M}_{acc}$ and the jet parameters n_e and $\dot{M}_{out}$ were given. However, this analysis was

tentative, and is now expanded and improved on here with new up-to-date procedures. The study of Par-Lup 3-4 was relevant to the question of the applicability of jet launching models at the lowest masses and one of the particular aims of the work presented here was to overcome difficulties with previous estimates of $\dot{M}_{out}/\dot{M}_{acc}$ in Par-Lup 3-4.

Firstly, tables of all the emission lines detected in the spectra of the two YSOs and their measured fluxes are presented. The goal here is to provide an important reference for future observational and computational studies of jets. Section 4.1 describes the line identification process and the tables of identified lines can be found in Appendix A. Secondly, the kinematics and morphology of the two jets are discussed in greater detail than in Bacciotti et al. (2011) (Sects. 4.2 and 4.3). For ESO-Hα 574, high spectral resolution UVES spectra taken from the ESO archive are included in order to improve the kinematical analysis. Since Bacciotti et al. (2011), several X-Shooter studies of accretion in YSOs have been conducted with participation from members of our team (Rigliaco et al. 2012; Alcalá et al. 2014; Manara et al. 2013). This experience has allowed us to refine our methods for estimating $\dot{M}_{acc}$. Hence, thirdly an updated analysis of $\dot{M}_{acc}$ in both targets is given, including a more detailed investigation of how the extinction of both sources can be evaluated and how it effects $\dot{M}_{acc}$ estimates (Sects. 4.4, 4.5). As both targets have edge-on disks, the obscuration effects of the disks are particularly relevant to our study of $\dot{M}_{acc}$. Furthermore, an improved approach for measuring $\dot{M}_{out}$ is presented along with a more accurate determination of $\dot{M}_{out}/\dot{M}_{acc}$ for both sources. Finally, the origin of the permitted emission in both sources is explored by examining their Balmer decrements (see Sect. 4.6).

2. Source properties

2.1. ESO-Hα 574

ESO-Hα 574 ($11^h16^m03^s7$, $-76°24'53''$) located in the Chamaeleon I star-forming region ($d = 160 \pm 17$ pc, Wichmann et al. 1998) is a low luminosity source with a derived spectral type of K8 (Comerón et al. 2004; Luhman 2007). Previous to this study it was known that ESO-Hα 574 powered a jet bright in many lines (HH 872 of total length 3150 AU) (Comerón & Reipurth 2006). The position angle (PA) of the jet is ~45° with up to 6 knots detected in the blue-shifted lobe (knots A to D) and a single knot, knot E in the red-shifted lobe (Bacciotti et al. 2011; Robberto et al. 2012). Robberto et al. (2012) used the Wide Field Planetary Camera on the HST to separate knot A into three separate knots which they label A1, A2, and A3. In the X-Shooter observations A2 and A3 are detected as one single knot labelled A1 by (Bacciotti et al. 2011) and A1 from Robberto et al. (2012) refers to knot A from Bacciotti et al. (2011). Also refer to Fig. 1 for further clarification on the naming of the knots.

The edge-on nature of the ESO-Hα 574 accretion disk was first reported in Comerón et al. (2004). The prediction of an edge-on disk for this star was based on the observation that the accretion signatures of ESO-Hα 574 were suppressed with respect to the outflow signatures suggestive of obscuration of the accretion zone by the disk. In addition, its bolometric luminosity is only 0.0034 $L_\odot$ (Luhman 2007), which, when compared with other typical T Tauri stars of the same spectral type (K8) in Chamaeleon I, makes this star under-luminous by a factor of about 150. This under-luminosity can be caused by an edge-on accretion disk. Finally the low radial velocities measured in the jet, as reported in Bacciotti et al. (2011), are typical of a star with
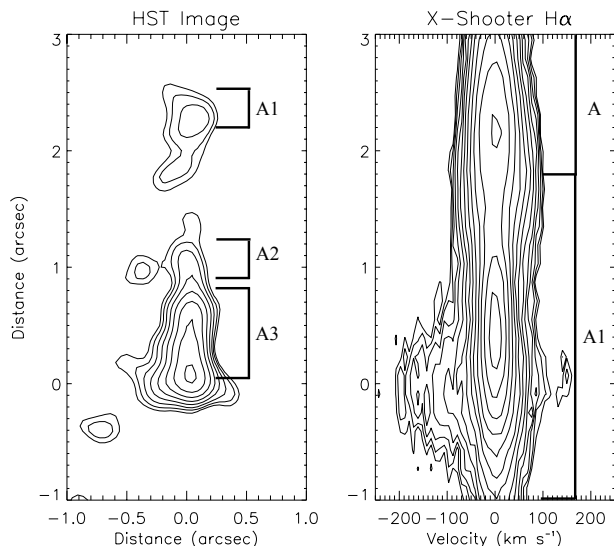
Fig. 1. Different notation systems for the knots of ESO-Hα 574 found in the literature. *Left*: HST WFPC images of ESO-Hα 574 published in Robberto et al. (2012). For the purpose of this figure we obtained the reduced image from the HST archive[1]. *Right*: position-velocity diagram of the ESO-Hα 574 jet in Hα made from our X-Shooter data and first published in Bacciotti et al. (2011). In this paper we follow the notation of Bacciotti et al. (2011).

an edge-on disk and therefore a jet which lies in the plane of the sky. The properties of ESO-HA 574 are very similar to TWA30 which is also a strong candidate for having an edge-on accretion disk. Looper et al. (2010a) discuss how the low radial velocities of the numerous forbidden emission lines (FELs) detected in the spectrum of TWA30, is evidence of an edge-on disk.

2.2. Par-Lup 3-4

Par-Lup 3-4 ($16^{\rm h}08^{\rm m}51^{\rm s}44$, $-39°05'30.5''$) found in the Lupus III cloud ($d = 200 \pm 40$ pc, Comeron et al. 2003), is a VLM object driving a small-scale jet at a PA of ~130° (HH 600) (Comerón & Fernández 2011). Its spectral type and mass have been estimated at M5 and 0.13 $M_\odot$ respectively (Comerón et al. 2003; Alcalá et al. 2014). The jet from Par-Lup 3-4 was first reported by Fernández & Comerón (2005). It was discovered using both spectroscopy and imaging and it is one of the lowest mass objects for which a jet has been directly imaged (Whelan et al. 2012). The source is under-luminous by ≈4 mag with respect to other M5 young stars in Lupus III (Comerón et al. 2003; Alcalá et al. 2014). Huélamo et al. (2010) model the SED (from the optical to submillimetre) of Par-Lup 3-4 and conclude that it also has an edge-on disk with an estimated inclination of 81° ± 6°. The fact that Par-Lup 3-4 has stronger accretion tracers than ESO-Hα 574 (Bacciotti et al. 2011) indicates that it may have a near edge-on disk, which is slightly more inclined than the ESO-Hα 574 disk.

3. Observations and data reduction

The X-Shooter observations presented in this paper were conducted on the VLT as part of the INAF X-Shooter GTO programme "An X-Shooter survey in star formation regions: low and sub-stellar mass objects" (085.C-0238(A), see Alcalá et al. (2011)). Both ESO-Hα 574 and Par-Lup 3-4 were observed on April 7 2010. For details of the observations and of the data reduction performed with the X-Shooter pipeline please refer to

---

[1] http://archive.stsci.edu/hst/

Bacciotti et al. (2011). Flux calibration was achieved using context LONG within MIDAS. For this purpose, a response function was derived by interpolating the counts/standard-flux ratio of the flux standards, observed the same night as the objects, with a third-order spline function, after airmass correction. The response function was then applied to the 1D spectra. Following the independent flux calibration of the X-Shooter arms, the internal consistency of the calibration was checked by plotting together the three spectra extracted from the source position and visually examining the superposition of overlapping spectral regions at the edge of each arm. For the observations of ESO-Hα 574, the UVB and VIS arms were found to be very well aligned, while the NIR arm presented a shift with respect to the VIS spectrum of ~25% lower. This was corrected for by scaling the NIR spectrum to the VIS continuum level. In the case of the Par-Lup 3-4 observations the alignment of the three arms was found to be very good and no re-scaling was necessary.

Previously unpublished UVES observations of ESO-Hα 574 (078.C-0429(A)) are also included in this paper. See Dekker et al. (2000) for a description of this instrument. The UVES spectra were obtained on December 12 2006 and the exposure time was 1000 s. A slit of width 1″ was again placed along the known jet PA. The resultant spectral resolution was ~40 000 for the UVES data and the pixel scale is 0.″182. The wavelength range of the UVES observation was approximately 4750 Å to 6850 Å but poor observing conditions meant that the jet is only detected in Hα, [O I]$\lambda\lambda6300$, 6363 and [S II]$\lambda\lambda6717$, 6731 with a good signal-to-noise ratio (~10). The seeing averaged 1.″5 during the observation. The UVES spectra were reduced using standard routines for bias subtraction, flat fielding, and wavelength calibration provided by IRAF.

4. Results

4.1. Line identification/flux measurement and summary of spectral characteristics

By placing the X-Shooter slit along the PAs of both jets and using the nodding mode the jet emission is traced to 8″ on either side of the driving source. For ESO-Hα 574 this includes knots A1 to B in the blue lobe and knot E in the red. The same labels for the knots as adopted by Bacciotti et al. (2011) are used here, and A2 and A3 from the notation of Robberto et al. (2012) are not resolved here. The full known extent of the Par-Lup 3-4 jet is covered by the X-Shooter slit. Emission lines were identified using the Atomic Line List database[2]. For the identification, we considered a wavelength uncertainty of about 0.5 Å. Nebular lines from abundant species having excitation energies below 40 000 cm^{-1} were firstly searched for, and only when identification with these criteria was not successful were permitted lines from neutral or single ionised atoms also considered. Line fluxes were computed through the Gaussian fitting of the line profiles after subtraction of the local continuum. Gaussian fitting was done using the IRAF task *splot*. Absolute flux errors were computed from the root mean square (rms) noise (measured in a portion of the spectrum adjacent to the line) multiplied by the spectral resolution element at the considered wavelength.

All the lines identified in the spectra of both targets along with the observed wavelengths and the lines fluxes are listed in Tables A1 and A2. In the case of ESO-Hα 574 (Table A1) the line fluxes are for the region of knot A1. Where emission lines are also detected in the other knots these fluxes are also given.

---

[2] http://www.pa.uky.edu/~peter/atomic/

The extraction regions for the knots A1, A, B, and E are $-1\rlap{.}''0$ to $1\rlap{.}''8$, $1\rlap{.}''8$ to $4\rlap{.}''2$, $5\rlap{.}''6$ to $7\rlap{.}''8$, and $-7\rlap{.}''5$ to $-5\rlap{.}''2$, respectively (also see Fig. 2). For Par-Lup 3-4 (Table A.2) the fluxes are measured from the spectrum extracted at the source position ($-0\rlap{.}''5$ to $0\rlap{.}''5$). A small number of lines are also seen in the Par-Lup 3-4 jet and for these lines the fluxes in the blue and red-shifted jets are measured over the regions $0\rlap{.}''5$ to $2\rlap{.}''4$ and $-0\rlap{.}''5$ to $-3\rlap{.}''3$, respectively. The line fluxes are not corrected for extinction and a discussion on estimating the extinction of ESO-Hα 574 and Par-Lup 3-4 is given in Sect. 4.4.

From studying Table A.1 it is clear that ESO-Hα 574 has a particularly rich spectrum. However, it is the abundance of jet lines that makes its spectrum so rich while the accretion tracers are not so common and those that are seen are weak. The ESO-Hα 574 jet is detected in many tens of emission lines, in species of hydrogen, oxygen, iron, sulphur, nitrogen, helium, and calcium for example, and in molecular lines of H_2. In Fig. 2 the position velocity (PV) diagrams of a selection of lines tracing the ESO-Hα 574 jet are presented. Numerous Balmer lines, although weak, are detected, while from the Paschen series only Paγ and Paβ are observed and no Brackett lines are present (Folha & Emerson 2001). Also note that the Ca II triplet is much fainter than would be expected for a CTTS which is driving such a powerful jet. Due to the weakness and absence of key accretion indicators, ESO-Hα 574 cannot be said to have a spectrum which is typical of a CTTS. However, its spectrum could be said to be characteristic of a CTTS with a disk with an inclination close to $90°$. Note the similarity of the ESO-HA 574 spectrum to that of TWA30, a YSO with an edge-on disk investigated by Looper et al. (2010a). While accreting YSOs with edge-on disks have been seen before, the effect of the disk obscuration on the accretion indicators is not often so stark. Thus these observations of ESO-Hα 574 are a good point of reference for future observations of similar YSOs. Par-Lup 3-4 has a spectrum which is typical of a young VLMS, in that all the usual accretion tracers are found while the jet is detected in only a handful of lines, e.g. [OI]$\lambda6300$, [SII]$\lambda6731$ (Whelan et al. 2009). Finally note that both sources show an abundance of Fe emission lines (Giannini et al. 2013). The full X-Shooter spectra of both targets are shown in Bacciotti et al. (2011).

4.2. Kinematics and morphology of the ESO-Hα 574 jet

Any kinematical study of the ESO-Hα 574 jet based on spectroscopic data is restricted by the edge-on nature of the ESO-Hα 574 disk and the resultant low inclination angle of the jet with respect to the plane of the sky. Outflows in the plane of the sky are characterised by low systemic radial velocities. This is especially true in the case of ESO-Hα 574, where the bulk of the jet emission lies along the 0 km s^{-1} line (Fig. 2). The low jet inclination angle was confirmed in Bacciotti et al. (2011) where spectroscopic observations of ESO-Hα 574 were compared to estimate the proper motions and thus tangential velocities and inclination angles of the knots. The effect of the low radial velocities on the kinematical analysis is compounded by the intermediate resolution of X-Shooter and for this reason archived UVES observations are also introduced here. Overall our discussion of the kinematics of the ESO-Hα 574 jet is confined to a discussion of asymmetries and of the shape of the Hα line profile.

4.2.1. Asymmetries in the jet

All four knots are only seen in a small fraction of the total number of lines which trace the jet, with the Hβ, Hα, [NII]$\lambda6583$,

and [SII]$\lambda6716, 6731$ lines providing the most kinematical information (refer to Fig. 2). While knots A1, A, and B lie close to 0 km s^{-1} there is an increase in radial velocity towards knot E of ~ 40 km s^{-1}. This is highlighted in Figs. 2 and 3. In Fig. 3 the extracted X-Shooter line profiles for the Hα and [SII]$\lambda6731$ lines are shown. The difference in velocity between the knots in the blue-lobe and knot E shows that the jet is asymmetric in velocity. The jet spectral profile is extracted at fixed points along the jet by spatially integrating the lines over the seeing full width half maximum (FWHM) of ~ 8 pixels. Gaussian fitting is then used to record the centroid velocity for each of the extracted profiles. In Fig. 4, PV diagrams of the [S II]$\lambda6731$, Hα, [N II]$\lambda6583$, and [O II]$\lambda6300$ emission line regions made from the UVES observations are displayed alongside extracted spectral lines profiles. Knots A1 and A are included in the observation however knots B and E are at the edge of the spatial coverage of the spectrum. Some noisy emission from B can be seen in the [SII]$\lambda6731$ PV diagram. While the bright knot of emission at the source position is centred at 0 km s^{-1}, note the presence of a blue-wing in the [S II]$\lambda6731$ and [NII]$\lambda6583$ lines which extends to ~ 40 km s^{-1}. This is evidence of some acceleration in the jet material with distance from the star, as seen for the red-lobe in the X-Shooter spectrum. The blue wing is also visible in the line profiles. Again the spectral profiles are extracted by summing over the seeing FWHM and were taken from the region at $\sim 1\rlap{.}''5$ from the source. The blue-wing is absent in the [O I]$\lambda6300$ line but this is due to an imperfect subtraction of the strong [O I]$\lambda6300$ sky line.

The spacing and number of the knots is also asymmetric in that there are several close knots in the blue-lobe which start at the source, while in the red lobe knot E at $\sim 6''$ is the first distinct emission knot. For protostellar jets, the blue-shifted jet is commonly observed to be the dominant lobe as the red-shifted flow is obscured by the disk within a few arcseconds of the driving source. However, in cases where the jet has a low inclination angle the obscuration is minimised and the red-shifted flow can be traced back to the star. Therefore, for ESO-Hα 574 it seems likely the observed asymmetry is as a result of the kinematics of the jet and points to differences in the rate at which the jet ejects material into both lobes and to differences in the medium into which the lobes are propagating. Variable ejection is commonly seen in jets and can be explained in terms of a pulsed jet model. Bonito et al. (2010) put forward a model of a jet ejected with variable velocity. The jet propagates into an inhomogeneous ambient medium with the inhomogeneity resulting from the knots ejected by the source interacting with the medium itself. A mutual interaction of knots arises from the random velocity of ejection of material at different epochs together with the strongly inhomogeneous medium into which each knot propagates. An irregular pattern of knots forms with detectable proper motion in a few years and with the spatial separation between consecutive knots being neither uniform in space nor constant in time. Differences in conditions in both lobes leads to differences in how they interact and thus differences between the two lobes. Jet asymmetries are discussed further in Sect. 5.2.

4.2.2. Hα line profile

As reported in Bacciotti et al. (2011), the Hα emission line region is made up of a narrow and broad component with the former made up of emission from the jet. These components are also detected in the UVES data (see Fig. 5) and in the He I line at 1.083 μm (Figs. 2, 5). Here the origin of the broad component is considered. Comparing the Hα red-shifted wing in the

X-Shooter Spectra of the ESO-HA 574 Jet
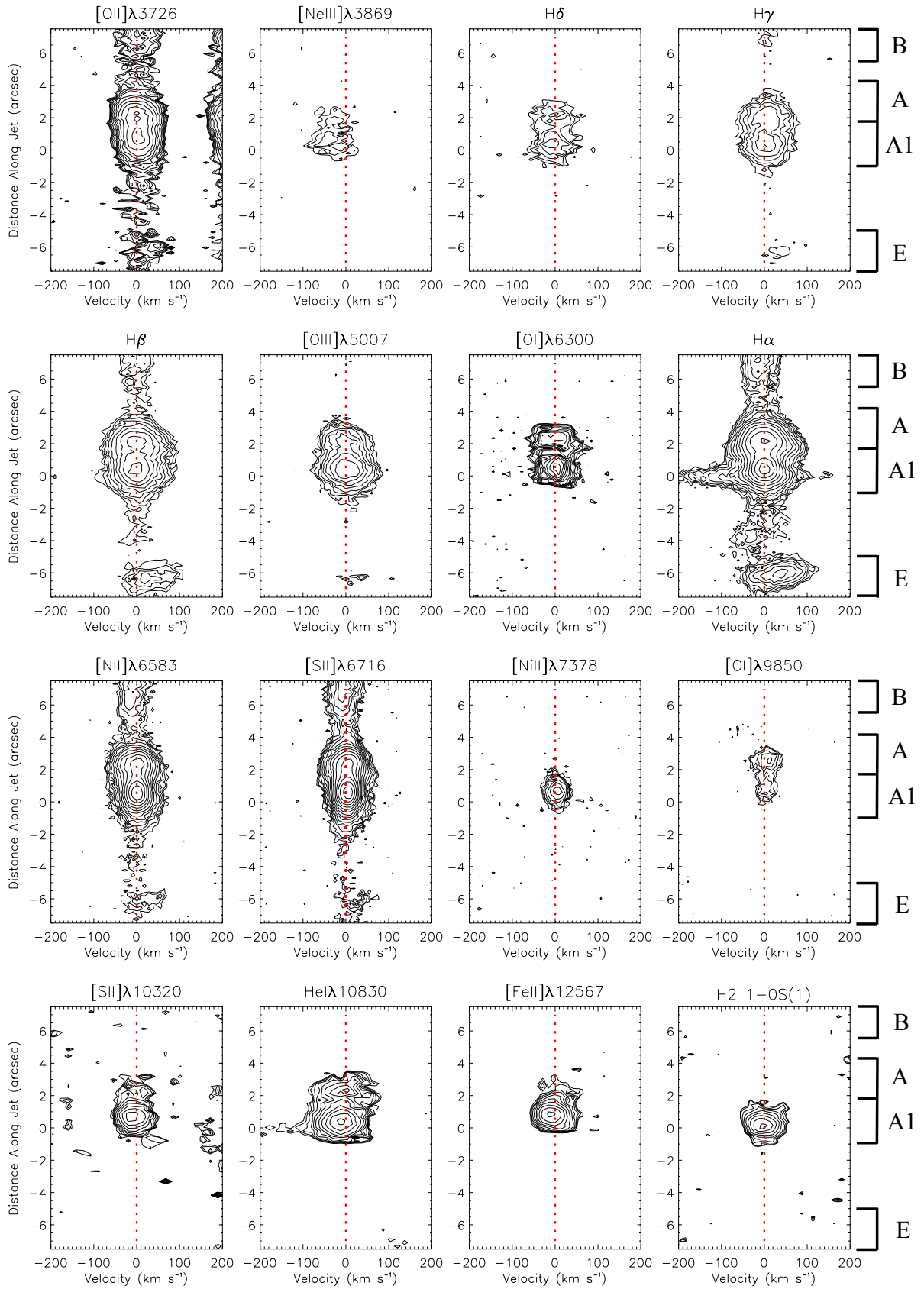

Fig. 2. Position velocity diagrams of the ESO-Hα 574 jet in some of the most interesting jet lines. Contours begin at 0.16×10^{-17} erg/s/cm^2 and increase logarithmically. Velocities are systemic. The positions and size of each knot are marked. The notation system of Bacciotti et al. (2011) is used. See Fig. 1 for the notation system of Robberto et al. (2012).
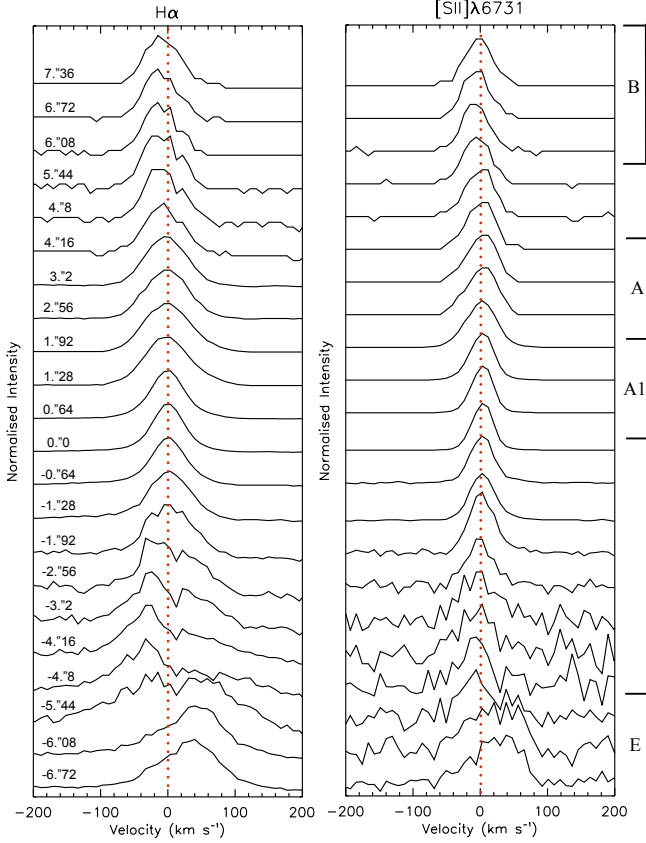
Fig. 3. Line profiles extracted in Hα and [SII]λ6731 from the X-Shooter spectra at various points along the length of the ESO-Hα 574 jet. While knot E at ∼−6.5″ is noisier than the blue-shifted part of the jet it has a higher velocity.
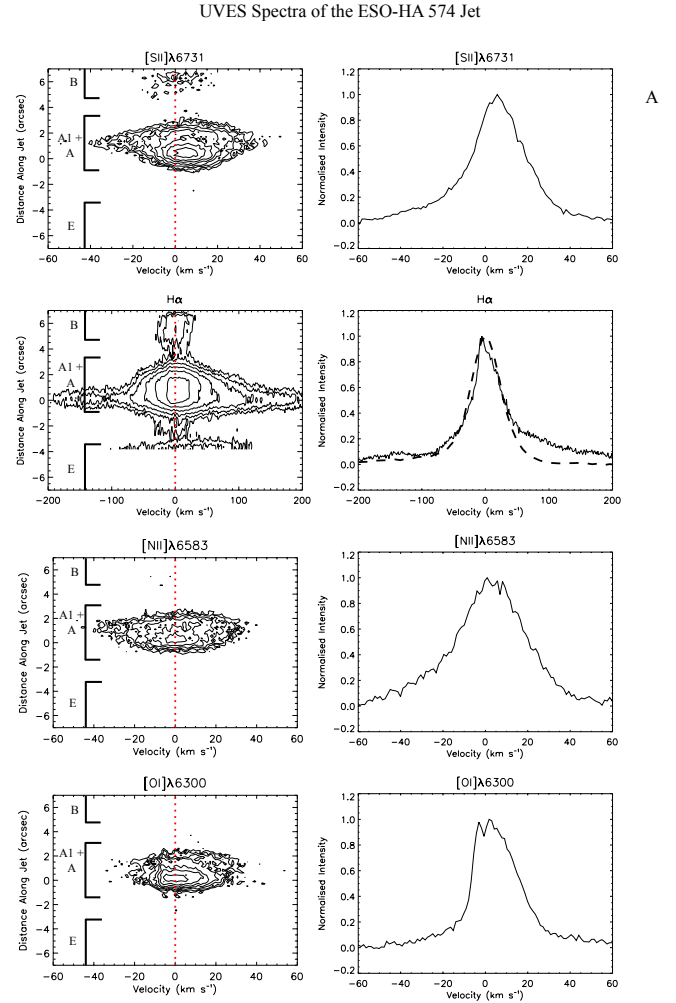

Fig. 4. Position velocity diagrams and line profiles of various lines in the ESO-Hα 574 jet made from UVES spectra taken in 2006. All velocities are systemic. Knots A1, A, and some of knots B and E are included in the data. Knots A1 and A are not resolved. Note that due to a difference of ∼3.3 yrs between this data and the X-Shooter data the knots here are closer to the source positions than in Fig. 2. Using the tangential velocities given in Table 1, we calculate that knots A, B, and E will have shifted by 0.″6, 0.″95, and 1.″4, respectively. The [S II]λ6731 and [N II]λ6583 lines regions have a blue-shifted wing which increases in velocity with distance from the source. In contrast to the Hα line region in the X-Shooter spectra the Hα line here has a more pronounced red-wing. For comparison the X-Shooter Hα line is over-plotted on the UVES profile as a dashed line. The [O I]λ6300 line region is slightly distorted from the subtraction of the [O I] sky line.

two observations of ESO-Hα 574 points to some red-shifted absorption in the Hα line in the X-Shooter observation. The HeI 1.083 μm line also exhibits such a red-shifted absorption or inverse P Cygni profile (IPC, see Fig. 5). This is a signature of infall onto the star (Fischer et al. 2008). Studies have shown that the profiles of permitted lines such as Hα, He I 1.083 μm, and Paβ can exhibit a variety of shapes which are explained by models incorporating both accretion and ejection scenarios (Whelan et al. 2004; Kurosawa et al. 2006; Fischer et al. 2008). While definite signatures of accretion and ejection such as IPCs and P Cygni (PC) profiles are seen in permitted lines some of the time, the broad width of the lines and high velocity line wings are a constant feature and high velocity symmetric wings up to ∼1000 km s^{-1} have been detected in the Hα lines of TTSs (Reipurth et al. 1996). Spectro-astrometry has been used to disentangle accretion and outflow components to permitted emission lines and has shown that the wings of the Hα line emission can originate in an outflow or wind (Takami et al. 2001; Whelan et al. 2004).

The case of ESO-Hα 574 is complex as the normally strong accretion tracers are very significantly suppressed and the emission line regions are dominated by the emission from the narrow jet. This is the opposite of what is normally seen in YSOs. Therefore it is difficult to say if the broad component is part of the accretion contribution to the total Hα emission region that becomes visible at the edges where the jet is no longer dominant, or is in fact a true line-wing tracing a wind. In Fig. 5 (top panel) the Hα line profiles of ESO-Hα 574 are compared to that of Par-Lup 3-4. As the shape of the Par-Lup 3-4 Hα line profile

is consistent with an origin in the accretion flow (Bacciotti et al. 2011), this comparison is done to illustrate the more complex nature of the ESO-Hα 574 line profile. Note that the width of the ESO-Hα 574 broad component is comparable to the width of the Par-Lup 3-4 Hα line suggesting that the broad component is perhaps more consistent with an accretion flow.

Bacciotti et al. (2011) performed a spectro-astrometric analysis of the wings of the ESO-Hα 574 and Par-Lup 3-4 Hα lines to check for an outflow contribution. Spectro-astrometry is a technique by which Gaussian fitting is applied to the point spread function (PSF) of a spectrum to measure spatial shifts with respect to the centroid of the continuum position. The accuracy to which these offsets can be measured depends on the signal-to-noise ratio (Whelan & Garcia 2008). The wing emission was found to be coincident with the continuum position
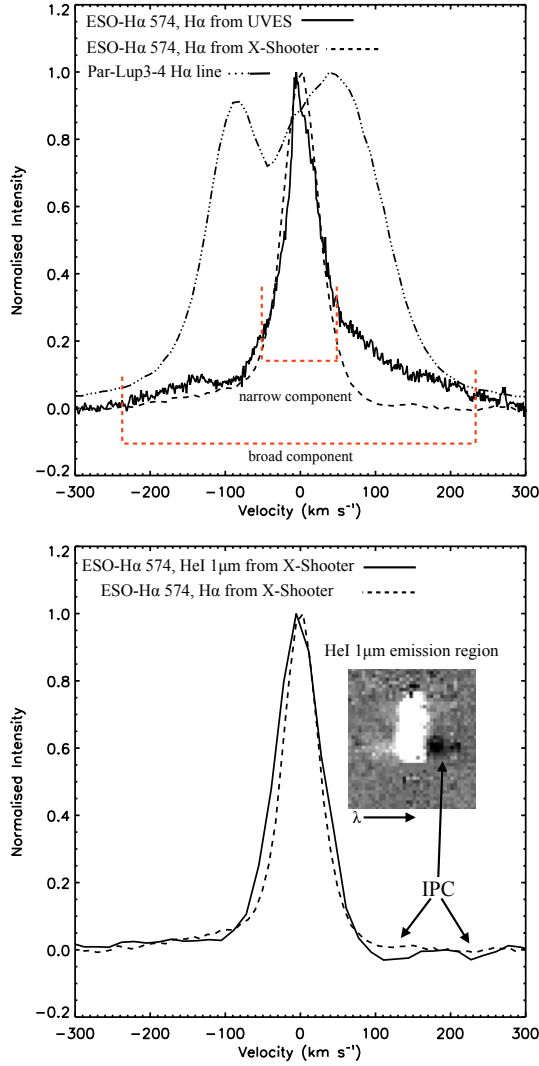
Fig. 5. *Top panel*: ESO-Hα 574 Hα line profiles as observed with X-Shooter and UVES compared to the Par-Lup 3-4 Hα line profile. The broad and narrow components of the ESO-Hα 574 line are marked. The red-shifted wing of the ESO-Hα 574 profile is much enhanced in the UVES data. *Bottom panel*: ESO-Hα 574 line profiles of He I at 1.083 μm and Hα (as observed with X-Shooter) compared to illustrate the presence of an IPC in the He I emission region. This is also seen in the 2D spectrum of ESO-Hα 574 (inset). In the section of the 2D spectrum shown, the continuum has been removed and as well as the IPC region and the jet region, faint blue-shifted emission is observed to the shortward of the jet.

and the analysis showed that any offset would be below the error in the analysis of ∼±40 mas for ESO-Hα 574 and ±20 mas for Par-Lup 3-4. In Fig. 6 the spectro-astrometric analysis of Bacciotti et al. (2011) is performed for the Hα emission region in the UVES spectrum. The full line is the offset before continuum subtraction, the dashed line after continuum subtraction and the 1σ error in the centroid measurements is ∼20 mas. The region between +140 km s^{-1} and −140 km s^{-1} is offset from the continuum position and therefore this region is dominated by emission from the outflow. The rest of the broad component beyond 140 km s^{-1} is coincident with the continuum position and therefore is likely dominated by emission from the infall. Overall we conclude that the broad component of the ESO-Hα 574 Hα region is likely made up of emission from infall and outflow. Also the comparison between the ESO-Hα 574 X-Shooter and
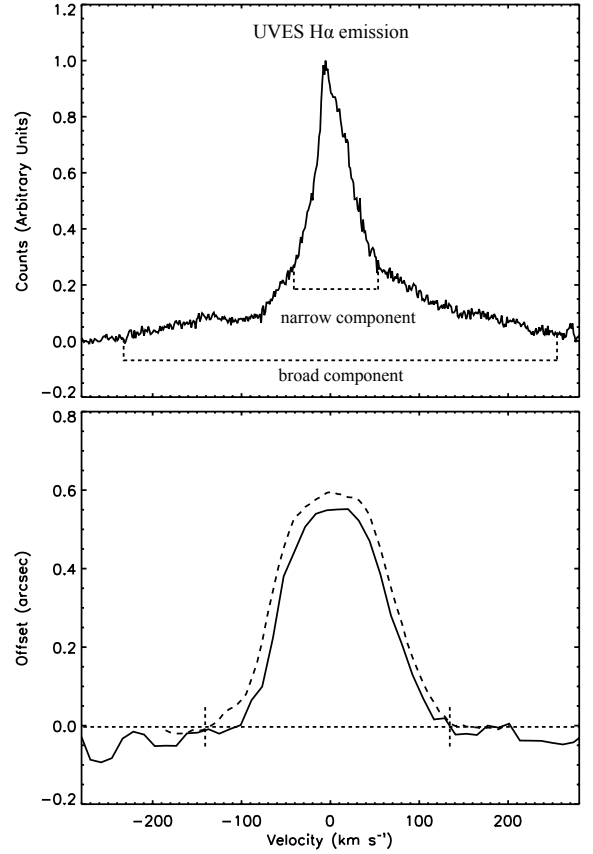

Fig. 6. Spectro-astrometry of the ESO-Hα 574 Hα emission in the UVES spectrum. *Upper panel*: UVES Hα line profile is shown and the narrow and broad components of the line are marked. *Lower panel*: Spectro-astrometric results are shown and the solid line is the analysis before continuum subtraction and the dashed line after continuum subtraction. The 1σ error is ∼20 mas. The Hα line is offset in the outflow between ±140 km s^{-1} and at least some of the broad component is found to be coincident with the stellar position.

UVES data does point to variability in the Hα emission region. This is based on the fact that the red-shifted wing is not detected in the X-Shooter spectrum. Variable accretion and outflow activity is a typical characteristic of YSOs (Costigan et al. 2012).

4.3. Kinematics of the Par-Lup 3-4 Jet

The low radial velocities measured in the Par-Lup 3-4 jet (±20 km s^{-1}) are consistent with the small inclination angle of the jet. Figure 7 presents the PV diagram of the Par-Lup 3-4 jet in the [SII]λ6731 line with the red crosses marking velocity centroid measured at fixed intervals along the jet. The line profiles corresponding to each red cross are also shown. The jet which extends to ±3″ on either side of the source displays few asymmetries in agreement with Comerón & Fernández (2011). Comerón & Fernández (2011) compare images of this jet with earlier observations and point out that the appearance of the jet is much more symmetric than in previous observations with both the blue and red-shifted lobes displaying similar intensities. They report the fading of the knot HH 600 between their 2003 and 2010 observations. HH 600 was observed in 2003 in the red-shifted lobe at a distance of 1″3 from Par-Lup 3-4 (Fernández & Comerón 2005). HH 600 is seen here in Fig. 7 at a distance of ∼2″5. It is clear from Fig. 7 that the radial velocity of the jet increases with distance from Par-Lup 3-4. An increase in radial velocity
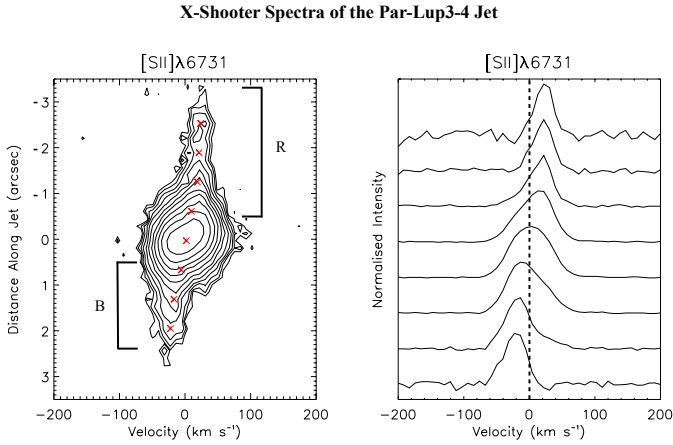
X-Shooter Spectra of the Par-Lup3-4 Jet

Fig. 7. Position velocity diagram of the Par-Lup 3-4 jet in [S II]λ6731 with the velocity centroid measured at various positions along the jet marked (red crosses). *Right panel*: line profiles corresponding to each red cross. Contours begin at 1.5×10^{-18} erg/s/cm^2 and increase logarithmically to 68×10^{-18} erg/s/cm^2. Velocities are systemic. The extraction window for the spectra of the blue and red jets are also shown. The fluxes of the lines which are detected in these regions of the jets are given in Table A.2. The Par-Lup 3-4 jet is fairly symmetric and clearly the velocity of both lobes increases with distance from the source. Comerón & Fernández (2011) note the presence of a small red-shifted knot at ~−2′′5 which is also seen here.

with distance from source has commonly been observed for jets driven by CTTSs (Davis et al. 2003) and is a feature of a magnetically driven flow (Whelan et al. 2004).

4.4. Estimates of extinction

An accurate estimate of the extinction is necessary for measuring $\dot{M}_{\rm acc}$ (from the luminosity of accretion indicators), and thus the ratio $\dot{M}_{\rm out}/\dot{M}_{\rm acc}$. However, for sources possessing an edge-on disk, like the ones under investigation here, this can be complicated by the scattering from the disk material, which can produce *grey extinction*, i.e. light suppression independent of wavelength (Mohanty et al. 2007). For ESO-Hα 574, Luhman (2007) estimated $A_{\rm J}$ = 0.45 mag meaning that the visual extinction (A_V) $\approx$ 1.7 mag. Literature values of A_V for Par-Lup 3-4 range from 2 mag to 5 mag, depending on the colours used to estimate reddening and an average of ~3.5 mag has been used in other studies (Comerón et al. 2003). In Bacciotti et al. (2011), using the above results, we adopted A_V = 3.5 mag and A_V = 1.7 mag for Par-Lup 3-4 and ESO-Hα 574, respectively.

One goal of the present work was to recover more accurate values for the extinction of both sources. This was done by comparing their spectra with the X-Shooter spectra of young zero-extinction Class III templates (Manara et al. 2013) of the same spectral type. The match was performed by applying to the template (i) a constant factor to normalise the flux and (ii) an reddening law to impose an artificial reddening and reproduce the slope of the observed spectrum. If the latter correction is zero, then extinction is most likely grey. Uncertainties in spectral types and in extinction of the templates lead globally to an error of <0.50 mag. Note however that veiling (especially strong in ESO-Hα 574) and dust scattering both increasing toward the blue, may still lead to an underestimation of the extinction. See also Alcalá et al. (2014).

The comparison was carried out as follows. The templates were normalised to the flux at 750 nm and then artificially reddened between A_V = 0...4.0 mag, in steps of 0.25 mag, until

the best match to the Par-Lup 3-4 and ESO-Hα 574 spectra was determined. It was found that a relative extinction correction of 1.5 mag is needed to best match the K8-type template to the spectrum of ESO-Hα 574, whereas no relative extinction is necessary to match the M5-type template to the spectrum of Par-Lup 3-4, suggesting that Par-Lup 3-4 is dominated by grey extinction. The extinction-corrected luminosity of ESO-Hα 574, however, is still considerably lower than the average luminosity of other YSOs of similar mass in Cha I-north. We argue therefore that ESO-Hα 574 is also affected by grey extinction. This is supported by the similarity of this system with the one of TWA30 described in Looper et al. (2010a,b). There is evidence that TWA 30A has an edge-on disk and it exhibits similar spectra to ESO-Hα 574, in that strong outflow tracers are detected but accretion tracers are relatively weaker.

In principle the adopted normalisation factor should be a measure of the obscuration of the source by the intervening disk. This could in fact be obtained by multiplying the flux ratio of the object to the template by the square of the ratio of their distances, assuming a similar stellar radius. The template and the object, however, are generally not in the same evolutionary stage and hence have different radii. Also, the uncertainties in distances are large. Therefore we keep with the approach of Bacciotti et al. (2011) and adopt a "grey" obscuration factor of approximately 150 and 25 for ESO-Hα 574 and Par-Lup 3-4, respectively. Bacciotti et al. (2011) obtained these values by comparing luminosities corrected for any relative extinction to the average luminosities of young stars of similar mass in the same star forming regions. Regarding the forbidden lines generated in the jets, however, we note that from analyses of infrared lines of Fe$^+$, Giannini et al. (2013) find that these regions are not affected by extinction. Therefore A_V = 0 is assumed for the diagnostics of physical conditions in the jets of both sources.

4.5. Estimates of $\dot{M}_{acc}$

As discussed in the Introduction, previous estimates of $\dot{M}_{\rm acc}$ for both ESO-Hα 574 and Par-Lup 3-4 were re-analysed. $\dot{M}_{\rm acc}$ is calculated from the equation,

$$\dot{M}_{\rm acc} = 1.25(L_{\rm acc}R_*)/(GM_*) \tag{1}$$

where $L_{\rm acc}$ is computed from $L_{\rm line}$ (Gullbring et al. 1998). $L_{\rm line}$ is the line luminosity derived from the measured fluxes after correction for relative extinction, and R_*, M_* are the stellar radius and mass. For both sources $L_{\rm line}$ was estimated from the line fluxes reported in Tables A.1 and A.2. So for ESO-Hα 574 it is the luminosity of the lines extracted from the region of knot A1. M_* and R_* are taken at 0.5 $M_\odot$ and 0.13 $M_\odot$, and at 0.12 $R_\odot$ and 0.18 $R_\odot$, for ESO-Hα 574 and Par-Lup 3-4, respectively. The values of L and $T_{\rm eff}$ used in the computation of R_* are taken from Merín et al. (2008) and Luhman (2007).

The new estimates differ from those presented in Bacciotti et al. (2011) due to the following factors. Firstly, improvements in the flux calibration mean that line fluxes and therefore values of $L_{\rm line}$ have changed. Early versions of the X-Shooter pipeline did not offer a reliable flux calibration but this situation has since been resolved. This was more of an issue for ESO-Hα 574, as fluxes are now found to be lower by a factor 4–5. Improvements in background and skyline subtraction, 1D extraction, and telluric correction also led to more accurate measurements of $L_{\rm line}$. Secondly, for the calculation of $L_{\rm line}$ only the line emission close to the source, i.e. knot A1 in the case of ESO-Hα 574 and the

arcsecond centred on the star in the case of Par-Lup 3-4, is considered. Previously, the emission extracted over the whole spatial range of the spectrum was considered. Thirdly, the new estimates of relative extinction described in the above paragraph have been applied using the extinction curves of Weingartner & Draine (2001). Finally, for the calculation of L_{acc} from L_{line} the new relationships described in Alcalá et al. (2014) are adopted. These relationships consider a combination of all the accretion indicators calibrated on sources for which the Balmer jump has been measured simultaneously.

The obscuration effect of the edge-on disks of both sources causing grey extinction is corrected for in the following way. At fixed mass Eq. (1) implies $\dot{M}_{acc} \propto L_{acc} \cdot L_*^{0.5}$, as the stellar radius goes as the square root of the luminosity. Assuming that the same obscuration factor suppresses both L_{acc} and L_*, $\dot{M}_{acc}$ is corrected using:

$$\dot{M}_{acc}(corrected) = (obscuration\,factor)^{1.5} * \dot{M}_{acc} \qquad (2)$$

where the obscuration factor was taken to be 150 and 25 for ESO-Hα 574 and Par-Lup 3-4, respectively, as described in Section 4.4. In Fig. 8, $\dot{M}_{acc}$ for ESO-Hα 574 and Par-Lup 3-4 is shown, with the black and red points resulting from the calculation before and after correction for the obscuration factor. Considering the corrected values, results put the mean accretion rate at $\log(\dot{M}_{acc}) = -9.15 \pm 0.45\ M_\odot\ \mathrm{yr}^{-1}$ for ESO-Hα 574 and $-9.30 \pm 0.27\ M_\odot\ \mathrm{yr}^{-1}$ for Par-Lup 3-4. The errors are the 1σ value marked in Fig. 8. $\dot{M}_{acc}$ for ESO-Hα 574 is at the lower end of the range of values of $\dot{M}_{acc}$ measured for other K type YSOs (Gullbring et al. 1998), and a factor ten lower than the approximate estimate in Bacciotti et al. (2011) with obscuration considered. The result for Par-Lup 3-4 is closer to our previous estimate in Bacciotti et al. (2011), and it is in agreement with previous results for M type YSOs (Antoniucci et al. 2011; Herczeg & Hillenbrand 2008; Hartigan et al. 1995).

These values of $\dot{M}_{acc}$ are compared in Sect. 4.6.3 with new estimates of $\dot{M}_{out}$. First note however, that additional uncertainties affect the $\dot{M}_{acc}$ estimate of ESO-Hα 574. For ESO-Hα 574 the accretion indicators are clearly dominated by jet emission. This can be seen in the PV plots of Fig. 2 where the emission peaks are always offset and also in the spectro-astrometric analysis presented in Fig. 6. Also refer to the discussion of the Balmer decrements in Sect. 4.6.1 below. This can lead to inconsistencies because, on one hand, the obscuration factor is estimated from the continuum radiation and not from the line emission, and on the other hand, the empirical relationships between L_{line} and L_{acc}, are derived from a sample of sources in Lupus (Alcalá et al. 2014) where L_{line} is actually dominated by accretion. As an attempt to quantify these caveats, L_{acc} is also derived using a linear correlation with an indirect tracer, i.e. the [OI]λ6300 line (Herczeg & Hillenbrand 2008). The [OI]λ6300 line is normally a strong tracer of protostellar jets and here we use the fact that empirical correlations between $\dot{M}_{acc}$ and [OI] λ6300 have shown that [OI] λ6300 indirectly traces accretion. As the [OI]λ6300 emission originates mostly in the extended regions, it is not affected by the obscuration of the disk and therefore one could expect $\dot{M}_{acc}$ derived from the [OI]λ6300 line to agree with the obscuration corrected values of $\dot{M}_{acc}$ derived from the accretion tracers. Thus $\dot{M}_{acc}$ calculated from the [OI]λ6300 line is a test of the accuracy of the obscuration correction. However, it should be kept in mind that the [OI]λ6300 correlation with L_{acc} is not perfect and Herczeg & Hillenbrand (2008) point out that the extended [OI]λ6300 emission may enter the slit only partially, which could account for the correlation scatter. In Fig. 8 it can be seen that the M_{acc}([O I]) result for Par-Lup 3-4 is perfectly
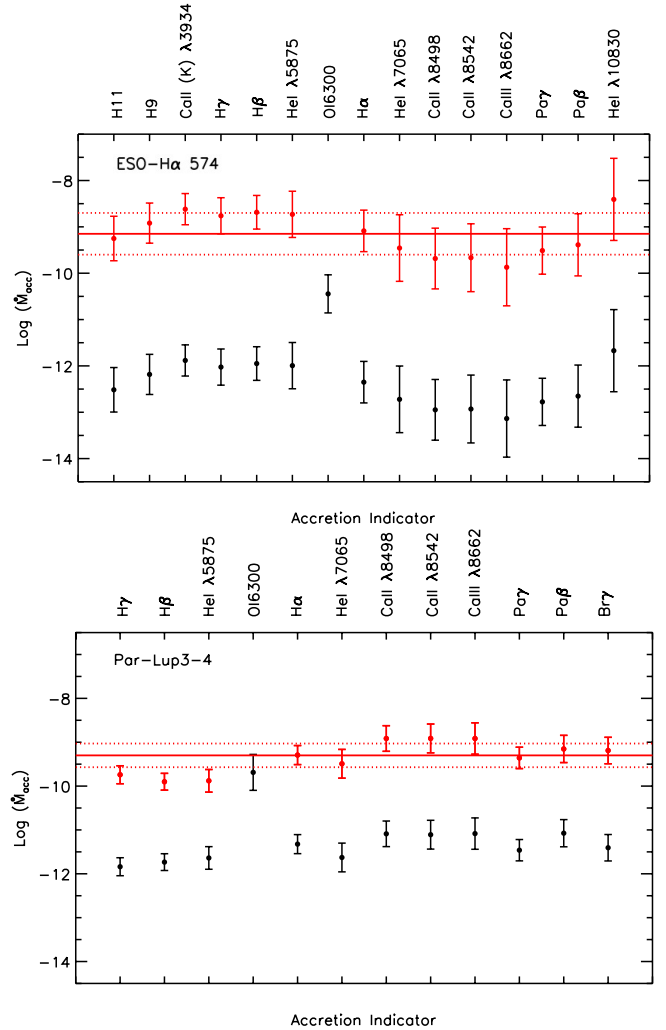
Fig. 8. Mass accretion rate calculated for various accretion indicators in ESO-Hα 574 (*top*) and Par-Lup 3-4 (*bottom*). The red points are the values of $\dot{M}_{acc}$ after correction for obscuration by the disk. [OI]λ6300 emission is an indirect indicator of accretion coming from extended regions and as such is blocked by disk. Therefore it is used as a test of the factor chosen to correct the other tracers for disk obscuration. The solid line gives the mean value of $\log(\dot{M}_{acc})$ and the dashed line is the $\pm 1\sigma$ uncertainty.

consistent with the corresponding values derived from the direct accretion tracers, corrected for obscuration. The comparison is not as good for ESO-Hα 574, however. The discrepancy may be alleviated considering that an imperfect sky line subtraction may have suppressed part of the [OI] flux. Furthermore, veiling and scattering close to the source may have actually affected the line, while here it is assumed to be seen under zero extinction conditions.

4.6. Physical properties of the gas and mass outflow rates

4.6.1. Diagnostics from hydrogen lines

In order to understand the physical conditions in the various emitting regions of ESO-Hα 574 and Par-Lup 3-4 the hydrogen emission from A1 and A in the ESO-Hα 574 flow and from Par-Lup 3-4 was investigated. A1 which covers the region $-0\rlap{.}''5$ to $1\rlap{.}''5$ also includes the emission from ESO-Hα 574 itself. Numerous HI emission lines are detected in the spectra of

Fig. 10. Balmer decrements for Par-Lup 3-4. Fluxes are extracted from the source spectrum. The decrements are fitted with Case B recombination (black and red lines) and LTE optically thin models (blue lines). The best fit is offered by the Case B scenario and $n_e = 10^{10}$ cm^{-3}, Te = 10 000 K. This is consistent with magneto-spheric accretion.

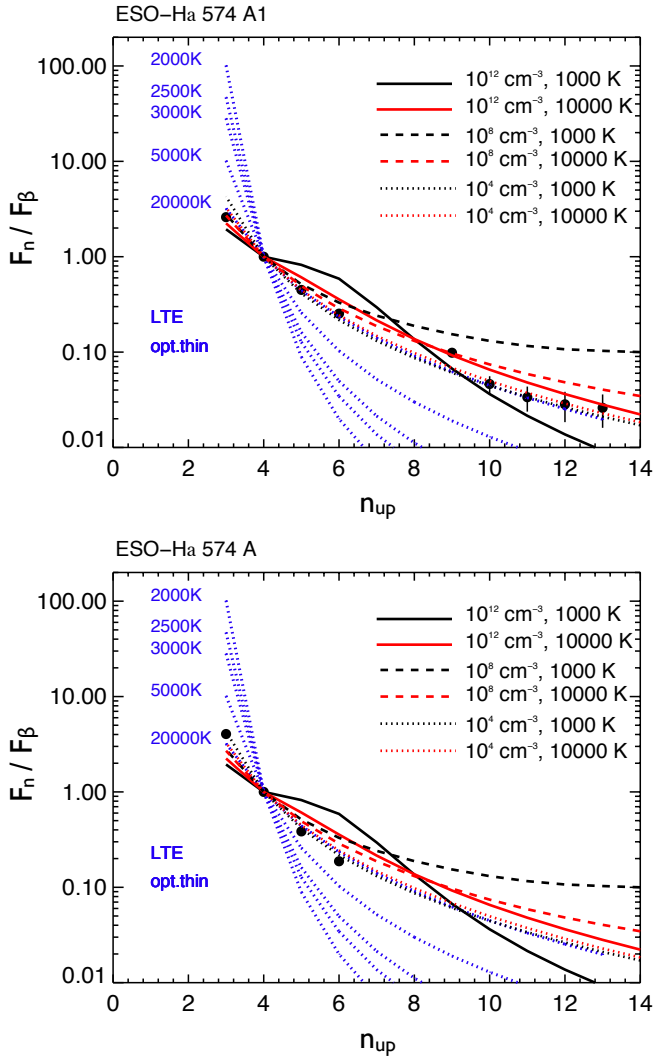**Fig. 9.** Balmer decrements for ESO-Hα 574, regions A1 (*top*) and A (*bottom*), fitted with Case B recombination (black and red lines) and LTE optically thin models (blue line). For the Case B scenario, the best fit is offered by $n_e = 10^4$ cm^{-3}, $T_e = 10\,000$ K. The LTE optically thin case with $T_e = 20\,000$ K provides an equally good fit. The results agree with the fact that for region A1, emission from the accretion zone is dominated by the outflow emission.

both sources and the Balmer decrements for ESO-Hα 574 A1, A and Par-Lup 3-4 were computed (with respect to Hβ). The line ratios are plotted as a function of their upper quantum number ($n_{\rm up}$) and results are presented in Figs. 9 and 10. While the spectral range of X-Shooter covers all of the Balmer lines, any lines with $n_{\rm up} > 13$ were found to be too noisy for inclusion in the analysis. Additionally, at the intermediate spectral resolution of X-Shooter the H7 and H8 lines are blended with other lines and are therefore also not included. It is noted that only the brightest Balmer lines were detected in knot A. To constrain the physical conditions in the emitting gas the decrements were firstly compared to standard Case B predictions (red and black curves) calculated for a range of temperature and density. The Case B curves were derived using the calculations of Hummer & Storey (1987) and the data files provided by Storey & Hummer (1995). These models assume that all lines are optically thin. Secondly, the decrements were also compared to optically thick and thin local thermodynamic equilibrium cases (LTE, blue curves) ratios, calculated over a temperature range of 2000 K to 20 000 K.
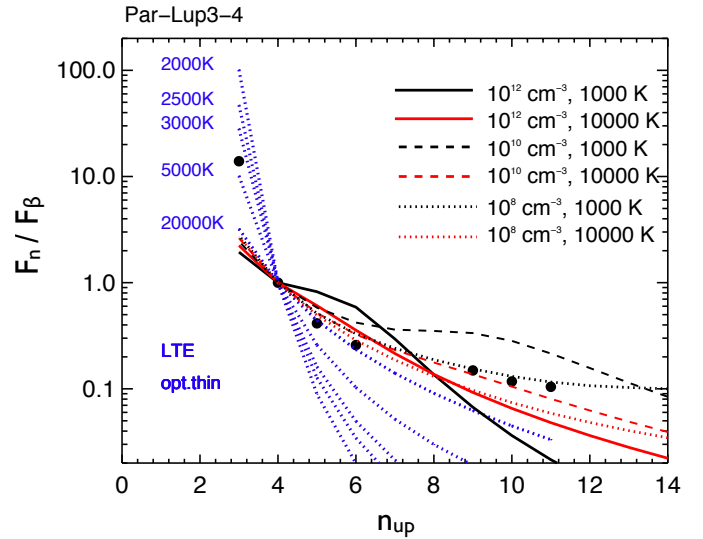
The optically thick case turned out not to be applicable, as it did not provide a good fit to the results, and it is not shown here.

For regions A1 and A in the ESO-Hα 574 outflow the Case B model for $n_e = 10^4$ cm^{-3}, $T_e = 10\,000$ K is a good fit to the decrements, as well as, for A1, the LTE optically thin curve with $T_e = 20\,000$ K. A density of $\sim10^4$ cm^{-3} and a temperature range of 10 000–20 000 K is consistent with an origin in a jet and also agrees with results published in other jet studies (Podio et al. 2011, 2008). This analysis shows that the bulk of the Balmer emission from A1 comes from the outflow, in agreement with the appearance of the PV diagrams of Fig. 2 and the spectro-astrometric analysis of the Hα line for this source (Fig. 6).

The gas from Par-Lup 3-4 is constrained with the Case B models, a high density of 10^8–10^{10} cm^{-3} and a temperature of $\sim10\,000$ K. Such temperatures and densities agree with an origin in magnetospheric accretion columns (Martin 1996). For example, Muzerolle et al. (2001) investigated magneto-spheric accretion in TTS and limited the temperature range of magneto-spherically accreting gas at 6000 K < T < 12 000 K, for 10^{-6} $M_\odot$ yr^{-1} ≥ $\dot{M}_{\rm acc}$ ≥ 10^{-10} $M_\odot$ yr^{-1}, where the lower gas temperatures correspond to sources with higher mass accretion rates. The origin of the Par-Lup 3-4 HI emission in accreting gas is in agreement with the spectro-astrometric analysis of the Hα line (Bacciotti et al. 2011).

The temperature estimated for Par-Lup 3-4 disagrees with the results of Bary et al. (2008) who found that the temperature of the gas emitting the Paschen and Brackett lines, in a sample of TTSs, was best fitted with a value of ≲2000 K. They argue that while this value is well below the temperature predicted by magnetospheric accretion models, the models do not currently allow for the absorption by the gas of high energy photons from the hot corona and/or accretion shocks. Inclusion of this method of heating and ionisation means that the low gas temperature can still be consistent with HI emission arising from accreting gas, as the ionising photons allow for the production of intense HI emission even at low temperatures. The majority of sources in the sample of Bary et al. (2008) have values of $\dot{M}_{\rm acc}$ on the order of 10^{-7} $M_\odot$ yr^{-1}, corresponding to the lower end of the temperature scale proposed by Muzerolle et al. (2001). While
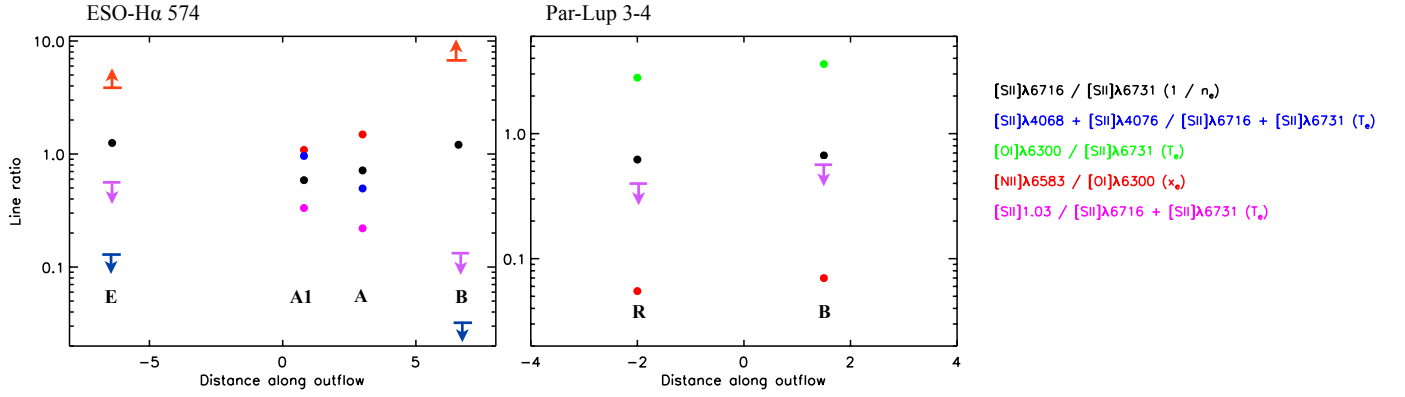
Fig. 11. Various line ratios tracing the excitation, n_e, T_e and x_e of the gas in ESO-Hα 574 A1, A, B and E and the Par-Lup 3-4 blue and red jets are plotted. As some lines were not detected in B and E and in the Par-Lup 3-4 jets upper limits of 3σ were assumed.

Table 1. Values of the different variables used in Eq. (3).

Object	v_t (km s^{-1})	l_t ($''$)	n_e (cm^{-3})	T_e (10^4 K)	x_e	$\dot{M}_{out}$ (10^{-10} $M_\odot$ yr^{-1})	$\dot{M}_{out}/\dot{M}_{acc}$
ESO HA 574							
Knot A1	130 ± 30	2.8	4500 ± 225	1.4 ± 0.2	>0.65	5.0 ± 1.5	
Knot A	130 ± 30	2.4	2100 ± 105	$''$	$''$	3.7 ± 1.1	0.5 (+1.0)(−0.2)
Knot B	220 ± 50	2.2	230 ± 11.5	$''$	$''$	8.2 ± 2.5	
Knot E	325 ± 50	2.3	160 ± 8.0	$''$	$''$	3.5 ± 1.1	0.3 (+0.6)(−0.1)
Par-Lup 3-4							
Blue	170 ± 30	1.9	4300 ± 200	3.1 ± 0.5	$(2.0 \pm 0.2) \times 10^{-3}$	0.3 ± 0.1	0.05 (+0.10)(−0.02)
Red	170 ± 30	1.8	4600 ± 300	2.4 ± 0.6	$(6.3 \pm 0.2) \times 10^{-3}$	0.29 ± 0.09	0.05 (+0.10)(−0.02)

Par-Lup 3-4 has a lower value of $\dot{M}_{acc}$, which suggests higher temperatures than for the sources in the study of Bary et al. (2008).

4.6.2. Diagnostics from ionic lines

In Giannini et al. (2013) the numerous [Fe II] and [Fe III] lines detected in our objects were used to derive the physical parameters (n_e, x_e and T_e) at the base of the ESO-Hα 574 and Par-Lup 3-4 jets. This paper pointed out the large gradients of physical conditions present in the post-shocked gas and that different lines/species probe different gas layers. Here, to further probe the gas in the two jets we employ the other line ratios sensitive to the gas physical conditions. The gas physical conditions are determined through a comparison of the observed values of the line ratios with values predicted theoretically using a numerical code that calculates the level population in a 5-level model atom (Bacciotti & Eislöffel 1999; Podio et al. 2006). Not all the lines, however, are present in a given knot, thus different combinations are used in the various positions. The values of the considered ratios or their upper/lower limits are plotted in Fig. 11 for knots A1, A, B and E of ESO-Hα 574 and for the jets in Par-Lup 3-4, and the results are given in Table 1.

For the ESO-Hα 574 outflow a combination of [SII] lines were used to estimate n_e and T_e independently from the abundance and ionisation of S. In particular for A1 and A the [SII]λ6716/[SII]λ6731 ratio, dependent strongly on n_e, and the ([SII]λ4068 +[SII]λ4076)/([SII]λ6716 + [SII]λ6731) ratio, dependent strongly on T_e, were used. Values of T_e around 1.4×10^4 K, and $n_e \sim 4500$, 2100 cm^{-3} were measured in A1 and A, respectively (see Table 1). Assuming the same temperature in the outermost knots we obtain $n_e \sim 230$ cm^{-3} in B and 160 cm^{-3} in E. Errors are 15% on the temperature and 5% on the electron

density. The ratio [NII]λ6583/[OI]λ6300, proportional to hydrogen ionisation fraction x_e, indicates $x_e > 0.65$ in the flow, and increases moving away from the source. This is in agreement with the value found on-source by Giannini et al. (2013). The high excitation of B and E would seem to contradict the non-detection of lines from higher ionisation lines such as [SIII] [OIII] in these knots (see Fig. 2), however we argue that this is due to the low electron density, not high enough to collisionally excite these lines. Note that the values retrieved on knot A1 are consistent with the estimates given in Giannini et al. (2013) for the analysis of the [SII] lines. At variance, iron lines, probing gas at different excitation in the post-shocked gas, provide a range of values for these parameters. Temperature (density) values from the [SII] lines are at the upper (lower) end of values derived from the iron lines.

For the Par-Lup 3-4 case the ratio [OI]λ6300/[SII]λ6731 was used in conjunction with [SII]λ6716/[SII]λ6731 and [NII]λ6583/[OI]λ6300, to find n_e, T_e, x_e within the framework of the so-called BE technique (Bacciotti & Eislöffel 1999; Podio et al. 2006). Here an improved BE procedure was used which considers the variation of T_e with the [SII]λ6716/[SII]λ6731 ratio. Note that the BE technique is not applicable to the ESO-Hα 574 outflow because of the presence of higher ionisation states of O and S close to the source, and absence of [OI]λ6300 in knots B and E. The results for the Par-Lup 3-4 jet at the source position and in the blue and red lobes are given in Table 1. Again the results are in agreement with the estimates of Giannini et al. (2013) deduced from [SII] lines.

For both sources the T_e sensitive ratio [SII] 1.03/([SII]λ6716 + [SII]λ6731) was also investigated. While only upper limits are detected for Par-Lup 3-4, overall results are consistent with the temperature being higher for Par-Lup 3-4 than for the ESO-Hα 574 outflow. On the other hand, the low level of hydrogen ionisation for Par-Lup 3-4 is confirmed by the ratio

of the [NI] and [NII] lines. The difference in the x_e and T_e values between ESO-Hα 574 and Par-Lup 3-4 can be explained in the context of a shock framework, as described for example in Hartigan et al. (1994). With reference to their Fig. 1, higher velocity shocks result in high x_e and high T_e at the shock front, but also a strong compression of the gas. As a result of the high density the gas cools quickly and the temperature of the post-shock region at the angular resolution of our observations is not very high. Alternatively, in low velocity shocks, where the gas has a low x_e, the compression is lower and the cooling is slower, thus the average temperature in the observed region has a higher valuer. Following this logic would mean that B and E in ESO-Hα 574 are higher velocity shocks than A1, A and the Par-Lup 3-4 jets. This explains why ESO-Hα 574 has a spectrum much richer in lines from high ionised species, such as [OIII] and [SIII], not detected in the Par-Lup 3-4 outflow. Hartigan et al. (1994) also plot the various line ratios as a function of shock velocity (see their Figs. 10 to 14). We used these models to estimate the shock velocities and found that for the Par-Lup 3-4 jets and ESO-Hα 574 inner knots, shock speeds of 30 km s^{-1} to 60 km s^{-1} are indicated, while speeds reach ~90 km s^{-1} in B and E of ESO-Hα 574.

4.6.3. Estimates of $\dot{M}_{out}/\dot{M}_{acc}$

The values of n_e and T_e given in Table 1 are now used to estimate $\dot{M}_{out}$. This is done through a comparison of the observed and theoretical line luminosity produced in a given forbidden line. To this aim the luminosity L_{SII} of the [SII]λ6731 line was considered in the separate knots making up the ESO-Hα 574 outflow and in the Par-Lup 3-4 blue and red jets. Following Nisini et al. (2005); Podio et al. (2006) we use the relationship

$$\dot{M}_{out} = \mu\, m_H\, (n_H\, V)\, v_t / l_t \qquad (3)$$

with $n_H V = L_{SII} \left(h\,\nu\, A_i\, f_i\, \frac{X^i}{X}\, \frac{X}{H} \right)^{-1}$. Here $\mu = 1.24$ is the mean atomic weight, m_H the proton mass, V the volume effectively filled by the emitting gas, v_t and l_t the tangential velocity and length of the knot, A_i and f_i the radiative rate and upper level population relative to the considered transition and finally $\frac{X^i}{X}$ and $\frac{X}{H}$ are the ionisation fraction and the relative abundance of the considered species. The tangential velocities of the knots as estimated in Bacciotti et al. (2011) are used here and the knot lengths are given in Sect. 4.1. These values are also given in Table 1. The S = S$^+$, elemental abundance is taken from Asplund et al. (2005), and the level population is calculated numerically as described in Podio et al. (2006). Note that the new estimate is more accurate than in Bacciotti et al. (2011), firstly due to the new values of the observed fluxes, that originate from an improved treatment of the flux calibration and the new extinction estimates. Secondly, and most importantly $\dot{M}_{out}$ is now calculated using the jet parameters derived directly from the spectra, rather than from an approximate formula based on the value of the critical density at an assumed unknown temperature, as was done previously for outflows from stars of very low mass.

These updated measurements of $\dot{M}_{out}$ and thus $\dot{M}_{out}/\dot{M}_{acc}$ are given in Table 1. $\dot{M}_{out}/\dot{M}_{acc}$ is derived for each lobe of the ESO-Hα 574 and Par-Lup 3-4 outflows by dividing by the average value of $\dot{M}_{acc}$. For the ESO-Hα 574 blue outflow, the average $\dot{M}_{out}$ of A1, A and B is used. From Table 1 it can be seen that in the case of ESO-Hα 574 the total (two-sided) $\dot{M}_{out}/\dot{M}_{acc}$ is higher than the maximum predicated by current models. However, errors are large for this source and may bring back the ratio within the limits. Furthermore as mentioned in

Sect. 4.5 it is likely that the effects of the edge-on disk of ESO-Hα 574 are still not full understood. Thanks to our revised analysis, the total (two-sided) $\dot{M}_{out}/\dot{M}_{acc}$ in Par-Lup 3-4 is now well within the limit of magneto-centrifugal jet launching models. The difference in the estimate of this ratio, as compared to results reported in Bacciotti et al. (2011) is mainly due to the reduction of the value of $\dot{M}_{out}$ (by one order of magnitude), when it is calculated with the correct formula for the population of the atomic levels at the diagnosed physical conditions, rather than with the approximate formula using the critical density at an assumed temperature of 8000 K. This result has important consequences for studies aimed at constraining this ratio in the substellar mass regimes. This is discussed further in Sect. 5.1 below.

4.7. Other jet emission lines

The spectrum of the ESO-Hα 574 jet contains a number of lines which have not been investigated as jet tracers as often as some of the traditional and well-studied jet tracers, such as the [NII]λ6583 or [SII]λ6731 lines for example. These lines warrant extra discussion.

HeI 1.083 μm: the He I 1.083 μm line traces high excitation regions (excitation energy of He I at 1.083 μm is 20 eV) and temperatures in excess of ~15 000 K. This line has been well studied in TTSs and has been found to have contributions from both the accretion onto the star (Fischer et al. 2008) and inner disk winds (Edwards et al. 2006). Confirmation that He I 1.083 μm emission traces disk winds came from the study of the line profiles i.e. the detection of PC profiles and from spectro-astrometric studies. For example Azevedo et al. (2007) use spectro-astrometry to detect an extended disk wind in the jet-less CTTS TW Hya. Observations of the He I 1.083 μm line in jets have been investigated far less frequently. Takami et al. (2002) present PV diagrams of the He I 1.083 μm emission in the DG Tau jet. They argue that shock heating must be the dominant heating mechanism in the jet in order to explain the presence of such a highly excited line. Ellerbroek et al. (2012) also detect He I 1.083 μm emission in the HH 1042 and HH 1043 jets. Thus ESO-Hα 574 is only one of a few jets where He I 1.083 μm has been identified to date. We would expect that future X-Shooter observations of jets would increase the number of jets for which this line is observed. The PV diagram of the ESO-Hα 574 He I 1.083 μm emission line region is presented in Fig. 1. Both knots A1 and A are detected while B and E are not seen (see discussion above). In Fig. 5 we show the He I 1.083 μm emission line profile and the emission region extracted from the 2D X-Shooter spectrum. The part of the line tracing the jet is narrow and has a velocity of ~0 km s^{-1} (as seen for the other jet lines). An IPC profile which can reveal important information about the accretion is also detected. For example, Fischer et al. (2008) discuss how red-shifted absorption features in the He I 1.083 μm line can reveal information about the accretion geometry of YSOs. Specifically they probed the geometry of magnetospheric accretion in CTTSs by modelling the red-shifted absorption at the He I 1.083 μm line via scattering of the stellar and veiling continua and found that the red-shifted absorption feature is sensitive to both the size of the magnetosphere of the star and the filling factor of the accretion shock. Finally some blue-shifted emission extending to ~200 km s^{-1} is also observed. See Sect. 4.2.2 for a discussion of the origin of this emission.

[NeIII]λ3869: the [NeIII]λ3869 line is observed in the spectrum of ESO-Hα 574 in the region of knot A1 (see Fig. 2). As the ionisation potential of Ne is high, high gas excitation is required. For

example Ne II to Ne III has an ionisation potential of 41.1 eV. Neon has been found to be excited in young stars in both high velocity shocks generated by outflows (van Boekel et al. 2009) and photo-evaporative disk winds (Pascucci & Sterzik 2009). In the sample of Pascucci & Sterzik (2009) transition disk objects are compared with younger more active systems and the authors conclude that the [Ne II] emission in the transition objects comes from the photo-evaporative wind while for the less evolved objects it is more likely to be generated by outflows. The shape and radial velocity of the Neon line can also help to distinguish between the two scenarios. If it is generated through outflow activity the line will be shifted with respect to the stellar rest velocity and will be comparable to FEL regions. If it has its origin in a photo-evaporative wind the line will be centred on the stellar rest velocity and likely asymmetric (Baldovin-Saavedra et al. 2012). From Fig. 1 it is clear that the most likely origin of the [NeIII]λ3869 line is in the ESO-Hα 574 jet. The line is blue-shifted to ~20 km s^{-1} and is extended to 2″. The radial velocity of this line is different from A1 as seen in the other jet tracers shown in Fig. 1, in that it is not symmetric about 0 km s^{-1} and is very definitely blue-shifted. This velocity of the [NeIII]λ3869 line is comparable to the blue-shifted wing seen in the UVES spectra and discussed in Sect. 4.2.1.

Refractory species: by studying the abundances of various refractory species in jets, the depletion onto dust grains and therefore the amount of dust present in the jets can be estimated (Podio et al. 2006). The amount of dust reflects the strength of the outflow shocks as the shocks will act to destroy the dust grains. ESO-Hα 574 has a particularly rich Fe spectrum described in Giannini et al. (2013). In addition, to the frequently investigated refractory species of Fe and Ca, C and Ni are also detected in the ESO-Hα 574 jet (see Fig. 2). Both knots A1 and A are detected in the [CI]$\lambda\lambda$9824, 9850 lines. The presence of strong [C I] lines implies low excitation conditions and therefore the non-detection of [C I] in B and E supports the results of Sect. 4.6, which show that B and E have a higher excitation that A1 and A (Nisini et al. 2005). Ni+ and Fe+ have similar ionisation potentials (7.9 and 7.6 eV, respectively) and critical densities and therefore they are expected to co-exist. From Fig. 2 it is seen that the [Ni II]λ7378 is only found in knot A1. Bautista et al. (1996) argue that strong [Ni II] emission has been explained by the contribution of fluorescent excitation in a low density environment and that the ratio between the [Ni II]λ7378 and [Ni II]λ7412 lines can be used to distinguish between shock and fluorescent excitation. Lucy (1995) show that in the case of fluorescence this ratio is ~4 but for shock excitation it is ~10. For ESO-Hα 574 [Ni II]λ7378/[Ni II]λ7412 = 13 ruling out fluorescence.

5. Discussion

5.1. Constraining $\dot{M}_{out}/\dot{M}_{acc}$ in BDs and VLMSs

The current sample of BDs and VLMSs with outflows is small and consists of ~10 objects (Joergens et al. 2013), ranging in mass from 0.024 $M_\odot$ to 0.18 $M_\odot$ (Whelan et al. 2012; Joergens et al. 2012a,b). Small spatial scales and the faintness of the jet emission limit the capability of studying these outflows with respect to the case of jets from CTTSs (Ray et al. 2007), however $\dot{M}_{out}/\dot{M}_{acc}$ has been investigated in some cases. The first investigations seemed to suggest that as mass decreases from from CTTSs to BDs, $\dot{M}_{out}/\dot{M}_{acc}$ may in fact increase from the 1% to 10% typically measured for CTTSs. If this trend is confirmed

it would present a challenge for current magneto-centrifugal jet launching models. For example, Ferreira et al. (2006) give an upper limit of 0.3 on the (one-sided) mass ejection to accretion ratio that can be sustained by a disk wind model and Cabrit (2009) discuss how high values of $\dot{M}_{out}/\dot{M}_{acc}$ are energetically challenging to stellar and x-wind models. Results from the first studies of $\dot{M}_{out}/\dot{M}_{acc}$ in BDs/VLMSs include, Whelan et al. (2009) where this ratio is estimated for the BDs ISO-Cha I 217, LS-RCr A1 and ISO-Oph 102. For all three objects $\dot{M}_{out}/\dot{M}_{acc}$ (one-sided) was measured to be ~1. More recently, Stelzer et al. (2013) report $\dot{M}_{out}/\dot{M}_{acc}$ for the blue-shifted outflow of the 0.050 $M_\odot$ BD FU Tau A to be ~0.3, Joergens et al. (2012b) measure $\dot{M}_{out}/\dot{M}_{acc}$ to be between 1% to 20% for the VLMS ISO 143 and in Bacciotti et al. (2011) we place this ratio for Par-Lup 3-4 in the range 0.3–0.5. It should be considered however that these investigations of accretion-ejection connection in BDs have had several limitations.

Firstly, BD jet velocities are not well constrained and estimates of the full jet velocity or at least of the tangential velocities are needed to calculate $\dot{M}_{out}$. Determination of the full jet velocity from the radial velocity is hampered by the uncertainty on the inclination angle of the system. Proper motion measurements are more accurate but they have been conducted only for the Par Lup 3-4 case. In other cases jet velocities have been inferred from the kinematics and shape of FEL profiles (Whelan et al. 2009). A second source of uncertainty is the estimate of n_e, normally derived from the [SII] lines. However, for BDs the [SII] lines have not been detected in majority of cases. A third factor is the reliability of estimates of $\dot{M}_{acc}$ which were often only derived using the Hα line. Additionally, the effect of extinction on the source (and thus estimate of $\dot{M}_{acc}$) and on the jet was not well known in most cases. Finally, and most significantly, methods for calculating $\dot{M}_{out}$ relied on uncertain values of the critical densities of the different jet tracers.

As studies of $\dot{M}_{out}/\dot{M}_{acc}$ in BDs are an important basis for comparing outflow activity in BDs and low mass stars it is essential that the difficulties outlined above are resolved. The revised analysis of $\dot{M}_{out}/\dot{M}_{acc}$ in Par-Lup 3-4 presented in the paper demonstrates how this can be done and hence this work is highly relevant to future studies of $\dot{M}_{out}/\dot{M}_{acc}$ in BDs and VLMSs. Indeed, for Par-Lup 3-4 $\dot{M}_{out}/\dot{M}_{acc}$ (one-sided) is reduced from ~0.25 to 0.05 as compared to results presented in Bacciotti et al. (2011). As the velocities of the Par-Lup 3-4 jets are well known from proper motion studies and as Par-Lup 3-4 contains sufficiently bright FELs for the jet parameters to be constrained Par-Lup 3-4 was an ideal source for constraining $\dot{M}_{out}/\dot{M}_{acc}$. Our analysis demonstrates the importance of understanding the effects of extinction and outlines an improved method for doing this. Furthermore, the importance of estimating $\dot{M}_{acc}$ from a range of tracers is clearly established along with the fact X-Shooter is currently one of the best instruments for doing this. Finally, the issue with uncertainties in critical density estimates is overcome through the use of the same exact calculation for $\dot{M}_{out}$ that is usually adopted for CTTSs jets. It is shown that the use of approximate formulas involving critical densities can lead to severe overestimates in $\dot{M}_{out}$ for $T_e > 8-9 \times 10^3$ K, thus introducing a strong bias and it is likely that this factor has lead to substantial over-estimations of $\dot{M}_{out}/\dot{M}_{acc}$ in early studies. It would be very beneficial to now revisit the BDs studied in Whelan et al. (2009) for example and investigate $\dot{M}_{out}/\dot{M}_{acc}$ in the same manner as done here for Par-Lup 3-4. Also note that studies aimed at measuring the proper motions and consequently velocities of known BD jets are currently under-way (Whelan et al. 2013).

5.2. Origin of ESO-Hα 574 jet asymmetries

Hirth et al. (1994) first began the discussion of asymmetries in protostellar jets. In their paper they presented the particular cases of the asymmetric jets driven by the CTTSs RW Aur and DO Tau. They also noted, that a literature search of protostellar jets known at the time, showed that in 50% of these jets the blue and red-shifted lobes were asymmetric in velocity. As well as velocity asymmetries the blue and red lobes of protostellar jets can also differ in their morphology and in the number of distinct knots (ESO-Hα 574), in the electron densities of the lobes (Caratti o Garatti et al. 2013; Podio et al. 2011) and in $\dot{M}_{out}$ (Whelan et al. 2009). While no dedicated observational study of asymmetric jets has been conducted since Hirth et al. (1994), numerous examples have been observed individually using state-of-the-art observing techniques (Dougados et al. 2000; Melnikov et al. 2009; Podio et al. 2011; Caratti o Garatti et al. 2013). This includes the asymmetric jet from the BD candidate ISO-ChaI 217 (Whelan et al. 2009; Joergens et al. 2012a). For the case of ISO-ChaI 217 the radial velocity of the red-shifted lobe was observed to be up to twice that of the blue-shifted lobe, however the exact magnitude of the velocity asymmetry will not be known until spectra taken along the derived jet PA become available. The red-shifted lobe was also found to be much brighter than the blue and the mass flux in the red flow was estimated at twice that of the blue flow. This is an interesting result as it highlights that the mechanism responsible for such asymmetries also operates at sub stellar masses. Observationally it seems that protostellar jets are more typically like ESO-Hα 574 and symmetric jets like Par-Lup 3-4 are observed less often.

In particular, jets which exhibit strong morphological symmetry, i.e. in the number and spacing of their knots are rare (Zinnecker et al. 1998) and even in cases where there are no velocity asymmetries it is normal that both lobes have different numbers of knots and that the spacing between these knots be variable. This is true for Par-Lup 3-4 where the jets are symmetric in velocity but a counterpart to the red-shifted knot HH 600 is not seen in the blue-shifted jet. Morphological asymmetries can be due to non-uniformities in the ambient medium and/or variability in the frequency at which material is ejected into the different lobes. A variable frequency and velocity of ejection (as discussed for ESO-Hα 574 in Sect. 4.2.1), differences in densities and in mass flux, can all be explained in terms of current jet models (Fendt & Sheikhnezami 2013; Matsakos et al. 2012). Matsakos et al. (2012) used numerical simulations to investigate the possibility that asymmetric jet velocities could be introduced either due to unaligned magnetic fields or when both lobes experienced different outer pressures. That is the cause is either intrinsic to the jet launching mechanism or extrinsic and originates due to inhomogenities in the ambient medium. Overall they found that both multi-polar magnetic moments and non-uniform environments could equally well explain the observed asymmetries. The idea of an inhomogeneous environment causing velocity asymmetries has been used before to explain cases of asymmetric jets where $\dot{M}_{out}$ is not found to be different in the two lobes (Podio et al. 2011; Melnikov et al. 2009). Fendt & Sheikhnezami (2013) also explore numerically methods for generating jet asymmetries which are intrinsic to the launch mechanism. To do this they begin with a highly symmetric jet and then disturb the symmetry in the disk to induce asymmetries in the jets. Interestingly they find that the disk asymmetries result in outflows where $\dot{M}_{out}$ can differ by up to 20% in the two lobes. Comparing $\dot{M}_{out}$ in the blue-shifted lobe of ESO-Hα 574 with $\dot{M}_{out}$ in the red-shifted lobe, it is seen that $\dot{M}_{out}$ red is ~60%

of $\dot{M}_{out}$ blue. Therefore this case would fit in well with the models of (Fendt & Sheikhnezami 2013). $\dot{M}_{out}$ blue is the average of $\dot{M}_{out}$ measured for knots A1, A and B while $\dot{M}_{out}$ red is the value measured for knot E

6. Summary

In this paper the accretion and outflow properties of ESO-Hα 574 and Par-Lup 3-4, derived from analysis of their X-Shooter spectra, are described. This analysis is a continuation of the preliminary study described in Bacciotti et al. (2011). Here the full set of data in all the different portions of the outflows, obtained after careful revision of the flux calibration and the effects of reddening, are presented. The application of improved diagnostics are described and, in particular, new and more accurate estimates of $\dot{M}_{out}/\dot{M}_{acc}$ to be compared with predictions of models of the jet launching are offered. ESO-Hα 574 represents an extreme example of a YSO with an edge-on accretion disk and a very rich spectrum of lines from high ionisation species. Thus, the treatment of this object presented here will be important for future studies of similar systems. Par-Lup 3-4 is one of a small sample of BDs and VLMSs known to drive jets. As Par-Lup 3-4 is the only object in this group where $\dot{M}_{out}/\dot{M}_{acc}$ has been estimated without large observational uncertainties, it is singularly important in the context of studies of jet launching at BD masses. Our main findings can be summarised as follows:

– The spectrum of ESO-Hα 574 contains an abundance of jet lines but weak accretion tracers, and some lines like Brγ are not present. It is hypothesised that the weakness of the accretion lines is due to the obscuration of the accretion zone by its edge-on accretion disk. This has been hypothesised for other YSOs whose spectra are rich in outflow lines but show comparatively weak accretion lines (Looper et al. 2010a). In comparison Par-Lup 3-4 has all the well-studied accretion lines (e.g. CaII triplet, Brγ) but a much smaller number of jet lines, of a lower excitation level. Par-Lup 3-4 is also postulated to have an edge-on disk but the comparison with ESO-Hα 574 in terms of accretion tracers points to its disk having a lower inclination. Tables of all the emission lines detected in both sources are given in Appendix A.

– A review of the kinematical properties of the ESO-Hα 574 jet is presented in Sect. 4.2. The low inclination of the jet means that what can be understood about the jet close to the driving source is limited. However, asymmetries are detected in the jet which can be explained in terms of differences in ejection rates between the two lobes. The ESO-Hα 574 Hα line region is interesting in that it has a prominent blue-wing in the X-Shooter spectrum and a stronger red-shifted wing in the UVES spectrum. The Hα line profile is divided into a narrow and a broad component. The narrow component is made-up of emission from the jet while the origin of the broad component is likely made up of emission from both infall and outflow. The Par-Lup 3-4 jet is far more symmetric than the ESO-Hα 574 jet.

– The extinction is an important quantity as it strongly affects measurements of $\dot{M}_{acc}$. By comparing the spectra of ESO-Hα 574 and Par-Lup 3-4 with X-Shooter spectra of zero extinction Class III templates, a relative extinction of 1.5 mag is estimated for ESO-Hα 574 while no relative extinction correction is needed for Par-Lup 3-4. The fact that the relative extinction-corrected luminosity of both sources is still considerably less than the average luminosity of other similar YSOs in their parent cloud suggests that they are affected

by grey extinction. This is due to obscuration by their disks and it is estimated that their luminosities are reduced by factors of 150 and 25 for ESO-Hα 574 and Par-Lup 3-4, respectively.

– Measurements of $\dot{M}_{acc}$ before and after obscuration correction are presented. The obscuration corrected values of $\log(\dot{M}_{acc})$ are -9.15 ± 0.45 $M_\odot$ yr^{-1} and -9.30 ± 0.27 $M_\odot$ yr^{-1} for ESO-Hα 574 and Par-Lup 3-4, respectively. By also estimating $\dot{M}_{acc}$ from the indirect indicator [OI]λ6300 *emitted from an extended region,* the obscuration factors can be tested. As $\dot{M}_{acc}$ from [OI] agrees with $\dot{M}_{acc}$ made from the direct accretion tracers and corrected for obscuration, the estimate of $\dot{M}_{acc}$ in Par-Lup 3-4 is likely accurate. For ESO-Hα 574 it is found that the obscuration correction does not completely solve the uncertainty in $\dot{M}_{acc}$. It is argued that veiling and scattering effects also impact on the extinction measurement.

– In Sect. 4.5 the Balmer decrements for the knots A1 and A in the ESO-Hα 574 flow, and for the Par-Lup 3-4 source spectrum are fitted with Case B and LTE optically thick and thin models. For A1 and A results are consistent with an origin in the jet. The spatial range of A1 includes emission from ESO-Hα 574 itself and this result further emphasises that the bulk of the emission in A1 comes from the outflow. For Par-Lup 3-4 the analysis shows that the decrements are best fitted with a Case B model with a density and temperature of 10^{10} cm^{-3} and 10 000 K. This is compatible with densities and temperatures derived for a magnetospheric accretion flow.

– Several line ratios are used to probe the ionisation, excitation, and temperature in knots A1, A, B, and E, and in the Par-Lup 3-4 red and blue jets. It is found that the ESO-Hα 574 jet is characterised by temperatures around 1.4×10^4 K and a hydrogen ionisation fraction >0.65, with knots B and E bearing the higher excitation. The electron density decreases from 4500 cm^{-3} to 160 cm^{-3} from inner to outer knots. In contrast, the Par-Lup 3-4 jet has a low degree of ionisation ($x_e = 2-6 \times 10^{-3}$), but a higher temperature ($2.5-3 \times 10^4$ K) and electron density (4000 cm^{-3}). These results explain why the ESO-Hα 574 has a spectrum much richer in lines from high ionised species than the Par-Lup 3-4 spectrum. The values of parameters found on-source are within the range of values derived by Giannini et al. (2013) from the analysis of the iron lines.

It is argued that no high excitation lines are detected in knots B and E of ESO-Hα 574, despite their high excitation, as the electron density is too low in these knots. B and E have a higher shock velocity that than either A1, A or both lobes of the Par-Lup 3-4 flow. This conclusion is borne out through comparison with the models of Hartigan et al. (1994).

– The improved diagnostic analysis and the adoption of an exact calculation based on a 5-level model atom allowed for an improved estimate (as compared to Bacciotti et al. 2011) of the mass outflow rate $\dot{M}_{out}$ in the jets. When $\dot{M}_{out}$ is combined with an updated estimate considering grey extinction of $\dot{M}_{acc}$, the estimate of the ratio $\dot{M}_{out}/\dot{M}_{acc}$ is also improved. For ESO-Hα 574, $\dot{M}_{out}/\dot{M}_{acc}$ in the red and blue flows is 0.5 (+1.0)(–0.2) and 0.3 (+0.6)(–0.1), respectively. For Par-Lup 3-4, $\dot{M}_{out}/\dot{M}_{acc}$ is 0.05 (+0.10)(–0.02) in both the red and blue flows. The improved estimate for Par-Lup 3-4 $\dot{M}_{out}/\dot{M}_{acc}$ is now within the range predicted by current jet launching models. The ESO-Hα 574 estimate still has large errors and it is not excluded that it lies within the limits predicted by models. Various biases which have likely affected

previous studies of $\dot{M}_{out}/\dot{M}_{acc}$ in BDs and VLMSs are discussed. The analysis of Par-Lup 3-4 offers an important example of how estimates of $\dot{M}_{out}/\dot{M}_{acc}$ in the lowest mass objects can be greatly improved by overcoming such biases. It should be noted however, that further improvements are needed, beyond the scope of this paper, to ensure that all biases have been overcome, e.g. the effects of scattering and veiling.

References

Asplund, M., Grevesse, N., & Sauval, A. J. 2005, Cosmic Abundances as Records of Stellar Evolution and Nucleosynthesis, 336, 25

Agra-Amboage, V., Dougados, C., Cabrit, S., Garcia, P. J. V., & Ferruit, P. 2009, A&A, 493, 1029

Alcalá, J. M., Stelzer, B., Covino, E., et al. 2011, Astron. Nachr., 332, 242

Alcalá, J. M., Natta, A., Manara, C. F., et al. 2014, A&A, 561, A2

Antoniucci, S., García López, R., Nisini, B., et al. 2011, A&A, 534, A32

Azevedo, R., Folha, D. F. M., Gameiro, J. F., & Calvet, N. 2007, ApJ, 670, 1234

Bacciotti, F., & Eislöffel, J. 1999, A&A, 342, 717

Bacciotti, F., Mundt, R., Ray, T. P., et al. 2000, ApJ, 537, L49

Bacciotti, F., Whelan, E. T., Alcalá, J. M., et al. 2011, ApJ, 737, L26

Baldovin-Saavedra, C., Audard, M., Carmona, A., et al. 2012, A&A, 543, A30

Bary, J. S., Weintraub, D. A., Shukla, S. J., Leisenring, J. M., & Kastner, J. H. 2008, ApJ, 678, 1088

Bautista, M. A., Peng, J., & Pradhan, A. K. 1996, ApJ, 460, 372

Bonito, R., Fridlund, C. V. M., Favata, F., et al. 2008, A&A, 484, 389

Bonito, R., Orlando, S., Peres, G., et al. 2010, A&A, 511, A42

Cabrit, S. 2009, in Protostellar Jets in Context, eds. K. Tsinganos, T. Ray, & M. Stute, Astrophysics and Space Science Proceedings Series (Berlin: Springer), 247

Cabrit, S. 2007, IAU Symp., 243, 203

Caratti o Garatti, A., Garcia Lopez, R., Weigelt, G., et al. 2013, A&A, 554, A66

Coffey, D., Bacciotti, F., Woitas, J., Ray, T. P., & Eislöffel, J. 2004, ApJ, 604, 758

Comerón, F., & Fernández, M. 2011, A&A, 528, A99

Comerón, F., & Reipurth, B. 2006, A&A, 458, L21

Comerón, F., Fernández, M., Baraffe, I., Neuhäuser, R., & Kaas, A. A. 2003, A&A, 406, 1001

Comerón, F., Reipurth, B., Henry, A., & Fernández, M. 2004, A&A, 417, 583

Costigan, G., Scholz, A., Stelzer, B., et al. 2012, MNRAS, 427, 1344

Davis, C. J., Whelan, E., Ray, T. P., & Chrysostomou, A. 2003, A&A, 397, 693

Dekker, H., D'Odorico, S., Kaufer, A., Delabre, B., & Kotzlowski, H. 2000, Proc. SPIE, 4008, 534

Dougados, C., Cabrit, S., Lavalley, C., & Ménard, F. 2000, A&A, 357, L61

Edwards, S., Fischer, W., Hillenbrand, L., & Kwan, J. 2006, ApJ, 646, 319

Eislöffel, J., & Mundt, R. 1995, Ap&SS, 233, 55

Ellerbroek, L. E., Kaper, L., Bik, A., Maaskant, K. M., & Podio, L. 2012, Circumstellar Dynamics at High Resolution, 464, 351

Fendt, C., & Sheikhnezami, S. 2013, ApJ, 774, 12

Fischer, W., Kwan, J., Edwards, S., & Hillenbrand, L. 2008, ApJ, 687, 1117

Fernández, M., & Comerón, F. 2005, A&A, 440, 1119

Ferreira, J. 2013, EAS Pub. Ser, 62, 169

Ferreira, J., Dougados, C., & Cabrit, S. 2006 A&A, 453, 785

Folha, D. F. M., & Emerson, J. P. 2001, A&A, 365, 90

Frank, A., Ray, T. P., Cabrit, S., et al. 2014 [arXiv:1402.3553]

Giannini, T., Nisini, B., Antoniucci, S., et al. 2013, ApJ, 778, 71

Gullbring, E., Hartmann, L., Briceno, C., & Calvet, N. 1998, ApJ, 492, 323

Hartigan, P., Morse, J. A., & Raymond, J. 1994, ApJ, 436, 125

Hartigan, P., Edwards, S., & Ghandour, L. 1995, ApJ, 452, 736

Herczeg, G. J., & Hillenbrand, L. A. 2008, ApJ, 681, 594

Hirth, G. A., Mundt, R., Solf, J., & Ray, T. P. 1994, ApJ, 427, L99

Hirth, G. A., Mundt, R., & Solf, J. 1997, A&AS, 126, 437

Huélamo, N., Bouy, H., Pinte, C., et al. 2010, A&A, 523, A42

Hummer, D. G., & Storey, P. J. 1987, MNRAS, 224, 801

Joergens, V., Pohl, A., Sicilia-Aguilar, A., & Henning, T. 2012a, A&A, 543, A151

Joergens, V., Kopytova, T., & Pohl, A. 2012b, A&A, 548, A124

Joergens, V., Herczeg, G., Liu, Y., et al. 2013, Astron. Nachr., 334, 159

Kurosawa, R., Harries, T. J., & Symington, N. H. 2006, MNRAS, 370, 580

Kwan, J., & Tademaru, E. 1995, ApJ, 454, 382

Looper, D. L., Mohanty, S., Bochanski, J. J., et al. 2010a, ApJ, 714, 45

Looper, D. L., Bochanski, J. J., Burgasser, A. J., et al. 2010b, AJ, 140, 1486

Luhman, K. L. 2007, ApJS, 173, 104

Lucy, L. B. 1995, A&A, 294, 555

Manara, C. F., Testi, L., Rigliaco, E., et al. 2013, A&A, 551, A107

Martin, S. C. 1996, ApJ, 470, 537

Matsakos, T., Vlahakis, N., Tsinganos, K., et al. 2012, A&A, 545, A53

McGroarty, F., Ray, T. P., & Froebrich, D. 2007, A&A, 467, 1197

Melnikov, S. Y., Eislöffel, J., Bacciotti, F., Woitas, J., & Ray, T. P. 2009, A&A, 506, 763

Merín, B., Jørgensen, J., Spezzi, L., et al. 2008, ApJS, 177, 551

Mohanty, S., Jayawardhana, R., Huélamo, N., & Mamajek, E. 2007, ApJ, 657, 1064

Monin, J.-L., Whelan, E. T., Lefloch, B., Dougados, C., & Alves de Oliveira, C. 2013, A&A, 551, L1

Muzerolle, J., Calvet, N., & Hartmann, L. 2001, ApJ, 550, 944

Nguyen, D. C., Scholz, A., van Kerkwijk, M. H., Jayawardhana, R., & Brandeker, A. 2009, ApJ, 694, L153

Nisini, B., Caratti o Garatti, A., Giannini, T., & Lorenzetti, D. 2002, A&A, 393, 1035

Nisini, B., Bacciotti, F., Giannini, T., et al. 2005, A&A, 441, 159

Pascucci, I., & Sterzik, M. 2009, ApJ, 702, 724

Podio, L., Bacciotti, F., Nisini, B., et al. 2006, A&A, 456, 189

Podio, L., Garcia, P. J. V., Bacciotti, F., et al. 2008, A&A, 480, 421

Podio, L., Eislöffel, J., Melnikov, S., Hodapp, K. W., & Bacciotti, F. 2011, A&A, 527, A13

Pudritz, R. E., Ouyed, R., Fendt, Ch., & Brandenburg, A. 2007, Protostars and Planets V, 231 Reipurth, eds. D. Jewitt, & K. Keil (Tucson: University of Arizona Press), 277

Ray, T., Dougados, C., Bacciotti, F., Eislöffel, J., & Chrysostomou, A. 2007, Protostars and Planets V, 231

Reipurth, B., Pedrosa, A., & Lago, M. T. V. T. 1996, A&AS, 120, 229

Rigliaco, E., Natta, A., Randich, S., et al. 2011, A&A, 526, L6

Rigliaco, E., Natta, A., Testi, L., et al. 2012, A&A, 548, A56

Robberto, M., Spina, L., Da Rio, N., et al. 2012, AJ, 144, 83

Shang, H., Li, Z.-Y., & Hirano, N. 2007, Protostars and Planets V, 261

Stelzer, B., Alcalá, J. M., Scholz, A., et al. 2013, A&A, 551, A106

Storey, P. J., & Hummer, D. G. 1995, VizieR Online Data Catalog: VI/64

Takami, M., Bailey, J., Gledhill, T. M., Chrysostomou, A., & Hough, J. H. 2001, MNRAS, 323, 177

Takami, M., Chrysostomou, A., Bailey, J., et al. 2002, ApJ, 568, L53

van Boekel, R., Güdel, M., Henning, T., Lahuis, F., & Pantin, E. 2009, A&A, 497, 137

Weingartner, J. C., & Draine, B. T. 2001, ApJ, 548, 296

Whelan, E., & Garcia, P. 2008, Jets from Young Stars II, 742, 123

Whelan, E. T., Ray, T. P., & Davis, C. J. 2004, A&A, 417, 247

Whelan, E. T., Ray, T. P., Podio, L., Bacciotti, F., & Randich, S. 2009, ApJ, 706, 1054

Whelan, E. T., Ray, T. P., Comeron, F., Bacciotti, F., & Kavanagh, P. J. 2012, ApJ, 761, 120

Whelan, E., Ray, T., Comeron, F., Bacciotti, F., & Kavanagh, P. 2013, Protostars and Planets VI, Heidelberg, July 15–20, Poster #1K033, 33

Zinnecker, H., McCaughrean, M. J., & Rayner, J. T. 1998, Nature, 394, 862

Appendix A: Tables of identified lines and line fluxes

Table A.1. ESO-Hα 574 emission line fluxes.

λ_{air} (Å)	Ion	Type	E_u (cm^{-1})	Knot	λ_{obs} (Å)	Flux ($\times 10^{-17}$ erg/s/cm^2)
	Identification					
3721.9^a	H I	14–2	109 119.2		3721.8	3.5 ± 0.5
3721.6^a	[S III]	$^1S_0$–$^3P_1$	27 161.00			
3726.0	[O II]	$^2D_{3/2}$–$^4S_{3/2}$	26 830.6		3726.0	76.8 ± 0.5
				A	3726.0	71.7 ± 0.5
				B	3726.0	18.3 ± 0.5
				E	3726.6	9.2 ± 0.5
3728.8	[O II]	$^2D_{5/2}$–$^4S_{3/2}$	26 810.6		3728.8	38.0 ± 0.5
				A	3728.8	46.7 ± 0.5
				B	3728.8	22.5 ± 0.5
				E	3729.0	13.3 ± 0.5
3734.4	H I	13–2	109 029.8		3734.3	1.3 ± 0.5
3750.2	H I	12–2	108 917.1		3750.3	1.4 ± 0.5
3769.9^a	[Co II]	a^3H_5–a^3F_3	27 469.1			1.7 ± 0.5
3770.2^a	Ti I	s^3F_4–a^3G_3	41 624.2			
3770.6	H I	11–2	108 772.3		3771.3	1.7 ± 0.5
3797.9	H I	10–2	108 582.0		3797.8	2.3 ± 0.5
3835.3	H I	9–2	108 324.7		3835.3	4.9 ± 0.5
3869.1	[Ne III]	$^1D_2$–$^3P_2$	25 838.7		3968.9	11.5 ± 0.5
3889.0	H I	8–2	107 965.1		3888.9	1.2 ± 0.5
3933.7	Ca II	$^2P_{3/2}$–$^2S_{1/2}$	25 414.4		3933.7	16.6 ± 0.3
3967.8	[Ne III]	$^1D_2$–$^3P_1$	25 838.7		3967.4	4.7 ± 0.3
3968.2^a	[Fe II]	$a^4G_{5/2}$–$a^6D_{3/2}$	26 055.4		3968.5	12.5 ± 0.3
3968.2^a	[Ti II]	$c^2D_{5/2}$–$a^4F_{3/2}$	25 192.8			
3968.4^a	Ca II	$^2P_{1/2}$–$^2S_{1/2}$	25 191.5			
3970.1	H I	7–2	107 440.5		3970.1	10.0 ± 0.3
				A	3970.1	3.35 ± 0.3
4068.6	[S II]	$^2P_{3/2}$–$^4S_{3/2}$	24 571.5		4068.6	149.0 ± 0.4
				A	4068.5	41.7 ± 0.4
4076.3	[S II]	$^2P_{1/2}$–$^4S_{3/2}$	24 524.8		4076.3	50.1 ± 0.4
				A	4076.3	15.9 ± 0.4
4101.7	H I	6–2	106 632.2		4101.8	13.4 ± 0.4
				A	4101.8	8.8 ± 0.4
4114.5	[Fe II]	$b^2H_{11/2}$–$a^4F_{9/2}$	26 170.2		4114.5	2.7 ± 0.4
4211.1	[Fe II]	$b^2H_{11/2}$–$a^4F_{7/2}$	26 170.2		4211.1	1.2 ± 0.4
4244.0	[Fe II]	$a^4G_{11/2}$–$a^4F_{9/2}$	25 428.8		4244.0	6.0 ± 0.5
4276.8	[Fe II]	$a^4G_{9/2}$–$a^4F_{7/2}$	25 805.3		4276.9	2.5 ± 0.5
4287.4	[Fe II]	$a^6S_{5/2}$–$a^6D_{9/2}$	23 317.6		4287.4	6.6 ± 0.4
4319.6	[Fe II]	$a^4G_{7/2}$–$a^4F_{5/2}$	25 981.6		4319.6	1.9 ± 0.3
4340.5	H I	5–2	105 291.7		4340.4	25.0 ± 0.4
				A	4340.5	18 ± 0.4
4346.9	[Fe II]	$a^4G_{11/2}$–$a^4F_{7/2}$	25 428.8		4346.6	0.7 ± 0.3
4347.4	[Fe II]	$b^4D_{5/2}$–$a^4D_{5/2}$	31 387.9		4347.6	1.0 ± 0.3
4352.8	[Fe II]	$a^4G_{9/2}$–$a^4F_{5/2}$	25 805.3		4352.8	1.0 ± 0.3
4359.3	[Fe II]	$a^6S_{5/2}$–$a^6D_{7/2}$	23 317.6		4359.3	4.8 ± 0.3
4362.7	C I	$^3D_3$–$^3D_3$	87 002.3		4362.5	0.8 ± 0.3
4363.2	[O III]	$^1S_0$–$^1D_2$	43 185.7		4363.4	3.0 ± 0.3
4413.8	[Fe II]	$a^6S_{5/2}$–$a^6D_{5/2}$	23 317.6		4413.8	3.1 ± 0.3
4416.3	[Fe II]	$b^4F_{9/2}$–$a^6D_{9/2}$	22 637.2		4416.3	4.4 ± 0.3
4432.4	[Fe II]	$b^4F_{5/2}$–$a^6D_{7/2}$	22 939.4		4432.7	1.6 ± 0.3
4438.9	[Fe II]	$b^4D_{1/2}$–$a^4D_{1/2}$	31 368.5		4439.2	1.0 ± 0.4
4452.1	[Fe II]	$a^6S_{5/2}$–$a^6D_{3/2}$	23 317.6		4452.2	2.8 ± 0.4
4457.9	[Fe II]	$b^4F_{7/2}$–$a^6D_{7/2}$	22 810.4		4457.9	2.3 ± 0.3
4471.7	He I	$^3D_1$–$^3P_0$	191 444.6		4471.5	4.0 ± 0.4
4571.1^a	K I	$^2D_{3/2}$–$^2P_{3/2}$	34 913.3		4571.5	3.2 ± 0.4
4571.1^a	Mg I]	$^3P_1$–$^1S_0$	21 870.5			
4580.8	[Cr II]	$a^4P_{3/2}$–$a^6S_{5/2}$	21 824.1		4580.8	1.4 ± 0.3
4607.0	[Fe III]	$^3F_3$–$^5D_4$	21 699.9		4606.8	1.0 ± 0.3
4658.1	[Fe III]	$^3F_4$–$^5D_4$	21 462.2		4658.1	9.2 ± 0.3

Notes. Fluxes refer to knot A1, are in units of erg/s/cm^2 $\times$ 10^{-17} and are not extinction corrected. Where the identified lines are also found in knots A, B or E the observed wavelengths and fluxes are also given. The regions over which the spectra for A1, A, B and E are extracted are shown in Fig. 2. The horizontal lines separate the UVB, VIS and NIR arms. $^{(a)}$ blended lines.

Table A.1. continued.

λ_{air} (Å)	Ion	Type	E_u (cm^{-1})	Knot	λ_{obs} (Å)	Flux ($\times 10^{-17}$ erg/s/cm^2)
		Identification				
4685.7	He II	4–3	41 1478.0		4685.7	2.1 ± 0.3
4701.5	[Fe III]	^{3}F$_3$–^{5}D$_3$	21 699.9		4701.6	3.4 ± 0.2
4713.4	He I	^{3}S$_1$–^{3}P$_0$	190 298.2		4713.4	1.0 ± 0.2
4728.1	[Fe II]	b^4P$_{3/2}$–a^6D$_{5/2}$	21 812.1		4728.1	1.0 ± 0.3
4733.0^a	Fe II]	^{6}D$_{5/2}$–y^4D$_{5/2}$	83 812.3		4733.0	0.7 ± 0.3
4733.0^a	Fe III]	^{3}F$_2$–^{1}F$_3$	118 163.6			
4733.9	[Fe III]	^{3}F$_2$–^{5}D$_2$	21 857.2		4734.1	1.5 ± 0.3
4754.7	[Fe III]	^{3}F$_4$–^{5}D$_3$	21 462.2		4755.0	2.2 ± 0.4
4769.4	[Fe III]	^{3}F$_3$–^{5}D$_2$	21 699.9		4769.6	1.8 ± 0.3
4774.7	[Fe II]	b^4F$_{7/2}$–a^4F$_{9/2}$	22 810.4		4774.4	1.1 ± 0.3
4777.7^a	[Fe III]	^{3}F$_2$–^{5}D$_1$	21 857.2		4777.7	1.0 ± 0.3
4778.0^a	[Fe II]	a^2D3/2–a^6D$_{7/2}$	21 308.0			
4798.3	[Fe II]	b^4P$_{3/2}$–a^6D$_{1/2}$	21 812.1		4798.0	0.7 ± 0.3
4814.5	[Fe II]	b^4F$_{9/2}$–a^4F$_{9/2}$	22 637.2		4814.5	3.7 ± 0.4
4861.3	H I	4–2	102 823.9		4861.3	63.2 ± 0.3
				A	4861.3	46.7 ± 0.3
				B	4861.4	10.8 ± 0.3
				E	4861.8	16.3 ± 0.3
4881.0	[Fe III]	^{3}H$_4$–^{5}D$_4$	40 481.9		4881.1	4.6 ± 0.4
4889.6^a	[Fe II]	b^4P$_{5/2}$–a^6D$_{7/2}$	20 830.6		4889.6	3.8 ± 0.3
4889.7^a	[Fe II]	a^2D$_{3/2}$–a^6D$_{3/2}$	21 308.0			
4905.3	[Fe II]	b^4F$_{7/2}$–a^4F$_{7/2}$	22 810.4		4905.4	2.0 ± 0.3
4930.5	[Fe III]	^{3}P$_0$–^{5}D$_1$	21 208.5		4930.5	1.2 ± 0.2
4931.2	[O III]	^{1}D$_2$–^{3}P$_0$	20 273.3		4930.8	0.9 ± 0.2
4950.7	[Fe II]	b^4F$_{3/2}$–a^4F$_{5/2}$	23 031.3		4950.7	0.9 ± 0.2
4958.9	[O III]	^{1}D$_2$–^{3}P$_1$	20 273.3		4958.9	11.6 ± 0.2
				A	4958.8	4.4 ± 0.2
4973.4	[Fe II]	b^4F$_{5/2}$–a^4F$_{5/2}$	22 939.4		4973.4	0.9 ± 0.2
4987.2	[Fe III]	^{3}H$_4$–^{5}D$_3$	20 481.9		4987.4	1.1 ± 0.2
5006.8	[O III]	^{1}D$_2$–^{3}P$_2$	20 273.3		5006.8	34.5 ± 0.3
				A	5006.7	14.7 ± 0.3
5011.3	[Fe III]	^{3}P$_1$–^{5}D$_2$	20 688.4		5011.2	2.2 ± 0.3
5015.7	He I	^{1}P$_1$–^{1}S$_0$	186 209.5		5015.8	1.3 ± 0.3
5111.6	[Fe II]	a^4H$_{11/2}$–a^4F$_{9/2}$	21 430.4		5111.5	2.1 ± 0.3
5158.8	[Fe II]	a^4H$_{13/2}$–a^4F$_{9/2}$	21 251.6		5158.7	15.7 ± 0.3
5164.0^a	[Fe II]	a^2F$_{7/2}$–a^4D$_{7/2}$	27 314.9		5164.4	2.0 ± 0.3
5164.5^a	[Cr II]	c^2F$_{7/2}$–a^4G$_{9/2}$	39 877.1			
5197.9	[N I]	^{2}D$_{3/2}$–^{4}S$_{3/2}$	19 233.2		5197.9	9.7 ± 0.3
				A	5197.9	4.5 ± 0.3
5200.3	[N I]	^{2}D$_{5/2}$–^{4}S$_{3/2}$	19 224.5		5200.3	6.4 ± 0.3
				A	5200.3	3.2 ± 0.3
5220.1	[Fe II]	a^4H$_{9/2}$–a^4F$_{7/2}$	21 581.6		5220.0	2.1 ± 0.4
5261.6	[Fe II]	a^4H$_{11/2}$–a^4F$_{7/2}$	21 430.4		5261.6	7.0 ± 0.3
5270.4	[Fe III]	^{3}P$_2$–^{5}D$_3$	19 404.8		5270.5	4.0 ± 0.3
5273.3	[Fe II]	b^4P$_{5/2}$–a^4F$_{9/2}$	20 830.6		5273.3	3.1 ± 0.3
5333.6	[Fe II]	a^4H$_{9/2}$–a^4F$_{5/2}$	21 581.6		5333.6	3.6 ± 0.3
5337.2	[Cr II]	c^4D$_{3/2}$–a^4D$_{3/2}$	38 362.4		5336.8	3.4 ± 0.3
5376.5	[Fe II]	a^4H$_{7/2}$–a^4F$_{3/2}$	21 711.9		5376.4	3.0 ± 0.3
5412.0^a	[Fe III]	^{3}P$_2$–^{5}D$_1$	19 404.8		5412.1	1.0 ± 0.3
5412.7^a	[Fe II]	a^2D$_{3/2}$–a^4F$_{5/2}$	21 308.0			
5413.3	[Fe II]	a^2H$_{11/2}$–a^4F$_{9/2}$	20 340.3		5413.1	1.2 ± 0.3
5527.3^a	[Fe II]	a^2D$_{5/2}$–a^4F$_{7/2}$	20 517.0		5527.2	4.3 ± 0.5
5527.6^a	[Fe II]	b^2P$_{1/2}$–a^4D$_{1/2}$	26 932.8			
5754.6	[N II]	^{1}S1$_0$–^{1}D$_2$	32 688.6		5754.4	5.9 ± 0.3
5875.9	He I	^{3}D$_1$–^{3}P$_0$	186 101.7		5875.9	8.1 ± 0.3
5890.1	Cr II]	^{6}D$_{3/2}$–v^4F$_{5/2}$	107 414.7		5890.2	5.3 ± 0.3
5896.0	Fe I	i^5D$_2$–x^5F$_2$	57 974.1		5896.0	2.3 ± 0.3
5980.1	Fe I]	x^1F$_3$–d^3F$_4$	53 763.3		5980.1	1.9 ± 0.3
6300.3	[O I]	^{1}D$_1$–^{3}P$_2$	15 867.9		6300.5	116.0 ± 0.2
				A	6300.5	56.3 ± 0.2
6312.1	[S III]	^{1}S$_0$–^{1}D$_2$	27 161.0		6312.3	4.7 ± 0.2

Table A.1. continued.

	Identification					
λ_{air} (Å)	Ion	Type	E_u (cm^{-1})	Knot	λ_{obs} (Å)	Flux ($\times 10^{-17}$ erg/s/cm^2)
6363.7	[O I]	$^1D_2-^3P_1$	15 867.9		6363.9	37.2 ± 0.2
				A	6364.0	14.3 ± 0.2
6548.0	[N II]	$^1D_2-^3P_1$	15 316.2		6548.2	43.6 ± 0.2
				A	6548.2	28.0 ± 0.2
				B	6548.1	4.1 ± 0.2
6562.8	H I	3–2	97 492.3		6562.9	248.1 ± 0.2
				A	6562.9	189.0 ± 0.2
				B	6562.8	41.2 ± 0.2
				E	6563.4	58.9 ± 0.2
6583.5	[N II]	$^1D_2-^3P_2$	15 316.2		6583.6	126.2 ± 0.2
				A	6583.6	83.9 ± 0.2
				B	6583.4	11.2 ± 0.2
				E	6583.4	6.0 ± 0.2
6678.2	He I	$^1D_2-^1P_1$	186 105.1		6678.3	1.5 ± 0.3
6716.4	[S II]	$^2D_{5/2}-^4S_{3/2}$	14 884.7		6716.6	206.9 ± 0.2
				A	6716.6	116.0 ± 0.2
				B	6716.4	26.7 ± 0.2
				E	6716.9	6.3 ± 0.2
6730.8	[S II]	$^2D_{3/2}-^4S_{3/2}$	14 852.9		6731.0	352.5 ± 0.2
				A	6731.0	162.0 ± 0.2
				B	6730.8	22.1 ± 0.2
				E	6731.4	5.0 ± 0.2
7065.7	He I	$^3S_1-^3P_0$	183 236.9		7065.4	0.8 ± 0.2
7135.8	[Ar III]	$^1D_2-^3P_2$	14 010.0		7136.0	3.5 ± 0.2
7155.2	[Fe II]	$a^2G_{9/2}-a^4F_{9/2}$	15 844.7		7155.3	26.9 ± 0.2
7172.0	[Fe II]	$a^2G_{7/2}-a^4F_{7/2}$	16 369.4		7172.1	7.4 ± 0.2
7291.5	[Ca II]	$^2D_{5/2}-^2S_{1/2}$	13 710.9		7291.6	20.2 ± 0.2
7319.9	[O II]	$^2D_{3/2}-^2P_{5/2}$	40 468.0		7320.1	45.1 ± 0.2
				A	7320.0	13.4 ± 0.2
7323.8	[Ca II]	$^2D_{3/2}-^2S_{1/2}$	13 650.2		7324.1	12.9 ± 0.2
7330.7	[O II]	$^2P_{3/2}-^2D_{3/2}$	40 468.0		7330.4	35.2 ± 0.2
7377.8	[Ni II]	$^2F_{7/2}-^2D_{5/2}$	13 550.4		7378.1	11.4 ± 0.2
7388.2	[Fe II]	$a^2G_{7/2}-a^4F_{5/2}$	16 369.4		7388.4	4.3 ± 0.2
7411.6	[Ni II]	$^2F_{7/2}-^2D_{3/2}$	14 955.6		7412.1	0.9 ± 0.2
7452.5	[Fe II]	$a^2G_{9/2}-a^4F_{7/2}$	15 844.7		7452.7	8.0 ± 0.2
7637.5	[Fe II]	$a^4P_{5/2}-a^6D_{7/2}$	13 474.4		7637.6	4.3 ± 0.2
7686.9	[Fe II]	$a^4P_{3/2}-a^6D_{5/2}$	13 673.2		7687.1	2.2 ± 0.2
7703.6^a	[Mn II]	$a^5G_5-a^5D_3$	27 571.3		7703.8	7.3 ± 0.3
7703.8^a	[Co II]	$c^3F_3-a^3H_4$	40 879.4			
8000.1	[Cr II]	$a^6D_{9/2}-a^6S_{5/2}$	12 496.4		8000.3	3.2 ± 0.2
8125.3	[Cr II]	$a^6D_{7/2}-a^6S_{5/2}$	12 303.9		8125.5	3.2 ± 0.2
8229.6	[Cr II]	$a^6D_{5/2}-a^6S_{5/2}$	12 147.8		8229.9	2.9 ± 0.2
8308.5	[Cr II]	$a^6D_{3/2}-a^6S_{5/2}$	12 032.6		8308.8	1.7 ± 0.2
8498.0	Ca II	$^2P_{3/2}-^2D_{3/2}$	25 414.4		8498.3	1.9 ± 0.2
8542.1	Ca II	$^2P_{3/2}-^2D_{5/2}$	25 414.4		8452.4	2.2 ± 0.2
8578.7	[Cl II]	$^1D_2-^3P_2$	11 653.6		8578.9	6.2 ± 0.2
8617.0	[Fe II]	$a^4P_{5/2}-a^4F_{9/2}$	13 474.4		8617.2	2.8 ± 0.2
8662.1	Ca II	$^2P_{1/2}-^2D_{3/2}$	25 191.5		8662.4	1.2 ± 0.2
8727.1	[C I]	$^1S_0-^1D_2$	21 648.0		8727.3	2.3 ± 0.3
8891.9	[Fe II]	$a^4P_{3/2}-a^4F_{7/2}$	13 673.2		8892.2	10.5 ± 0.2
9033.5	[Fe II]	$a^4P_{1/2}-a^4F_{5/2}$	13 904.8		9033.7	4.2 ± 0.4
9051.9	[Fe II]	$a^4P_{5/2}-a^4F_{7/2}$	13 474.4		9052.2	7.8 ± 0.2
9068.6	[S III]	$^1D_2-^3P_1$	11 322.7		9069.2	21.6 ± 0.3
9123.6	[Cl II]	$^1D_2-^3P_1$	11 653.6		9123.7	2.2 ± 0.3
9226.6	[Fe II]	$a^4P_{3/2}-a^4F_{5/2}$	13 673.2		9226.8	7.4 ± 0.2
9267.6	[Fe II]	$a^4P_{1/2}-a^4F_{3/2}$	13 904.8		9267.7	5.6 ± 0.3
9530.6	[S III]	$^1D_2-^3P_2$	11 322.7		9531.2	64.9 ± 0.3
				A	9530.9	16.4 ± 0.3
9824.1	[C I]	$^1D_2-^3P_1$	10 192.6		9824.5	4.0 ± 0.3
9850.3	[C I]	$^1D_2-^3P_2$	10 192.6		9850.6	11.4 ± 0.3
12 086.7	[S II]	$^2P_{3/2}-^2D_{3/2}$	24 571.5		10 286.5	50 ± 1

Table A.1. continued.

λ_{air} (Å)	Ion	Type	E_u (cm^{-1})	Knot	λ_{obs} (Å)	Flux ($\times 10^{-17}$ erg/s/cm^2)
				A	10 286.6	20 ± 1
10 320.5	[S II]	^{2}P$_{3/2}$–^{2}D$_{5/2}$	24 571.5		10 320.4	64 ± 1
				A	10 320.4	20 ± 1
10 336.4	[S II]	^{2}P$_{1/2}$–^{2}D$_{3/2}$	24 524.8		10 336.3	50 ± 1
				A	10 336.3	14 ± 1
10 370.5	[S II]	^{2}P$_{1/2}$–^{2}D$_{5/2}$	24 524.8		10 370.4	22 ± 1
				A	10 370.4	7 ± 1
10 397.7^a	[N I]	^{2}P$_{3/2}$–^{2}D$_{5/2}$	28 839.3		10 398.0	4 ± 1
10 398.2^a	[N I]	^{2}P$_{1/2}$–^{2}D$_{5/2}$	28 838.9			
10 407.2^a	[N I]	^{2}P$_{3/2}$–^{2}D$_{3/2}$	28 839.3		10 407.2	3 ± 1
10 407.6^a	[N I]	^{2}P$_{1/2}$–^{2}D$_{3/2}$	28 838.9			
10 830.3	He I	^{3}P$_1$–^{3}S$_1$	169 087.0		10 830.1	132.7 ± 0.8
				A	10 830.3	56.2 ± 0.3
10 938.0	H I	0–3	106 632.2		10 937.8	14.5 ± 0.8
11 618.9	[Ti II]	a^2G$_{7/2}$–a^4F$_{9/2}$	8997.7		11 618.9	6 ± 1
12 485.4	[Fe II]	a^4D$_{5/2}$–a^6D$_{7/2}$	8391.9		12 484.9	2.3 ± 0.4
12 566.8	[Fe II]	a^4D$_{7/2}$–a^6D$_{9/2}$	7955.3		12 566.6	82.7 ± 0.7
				A	12 566.4	16.7 ± 0.2
12 610.9	[Cr I]	a^5D$_2$–a^7S$_3$	7927.5		12 611.0	3 ± 1
12 787.8	[Fe II]	a^4D$_{3/2}$–a^6D$_{3/2}$	8680.45		12 787.5	11 ± 2
12 818.1	H I	5–3	105 291.7		12 817.7	13 ± 1
12 942.7	[Fe II]	a^4D$_{5/2}$–a^6D$_{5/2}$	8391.9		12 942.5	13.8 ± 0.8
12 977.7	[Fe II]	a^4D$_{3/2}$–a^6D$_{1/2}$	8680.4		12 977.8	3.7 ± 0.8
13 205.5	[Fe II]	a^4D$_{7/2}$–a^6D$_{7/2}$	7955.30		13 205.3	26.9 ± 0.8
13 277.8	[Fe II]	a^4D$_{5/2}$–a^6D$_{3/2}$	8391.9		13 277.8	9.5 ± 0.9
15 334.7	[Fe II]	a^4D$_{5/2}$–a^4F$_{9/2}$	8391.9		15 334.4	13.9 ± 0.6
15 994.7	[Fe II]	a^4D$_{3/2}$–a^4F$_{7/2}$	8680.5		15 994.7	14.4 ± 0.5
16 435.5	[Fe II]	a^4D$_{7/2}$–a^4F$_{9/2}$	7955.3		16 435.3	72.5 ± 0.7
16 637.7	[Fe II]	a^4D$_{1/2}$–a^4F$_{5/2}$	8846.8		16 637.4	7.2 ± 0.6
16 768.8	[Fe II]	a^4D$_{5/2}$–a^4F$_{7/2}$	8391.9		16 768.1	16.7 ± 0.6
17 475.0	H$_2$	1-0S(7)			1.74746	9.3 ± 0.9
17 971.0	[Fe II]	a^4D$_{3/2}$–a^4F$_{3/2}$	8680.5		17 970.7	4 ± 1
18 093.9	[Fe II]	a^4D$_{7/2}$–a^4F$_{7/2}$	7955.3		18 093.5	16 ± 2
19 570.2	H$_2$	1-0S(3)			19 570.8	69.7 ± 0.2
21 212.5	H$_2$	1-0S(1)			21 212.5	39.2 ± 0.2
22 226.8	H$_2$	1-0S(0)			22 227.0	8.4 ± 0.3
22 471.0	H$_2$	2-1S(1)			22 470.0	4.8 ± 0.3

Table A.2. Par-Lup 3-4 emission line fluxes.

λ_{air} (Å)	Ion	Type	E_u (cm^{-1})	Jet	λ_{obs} (Å)	Flux ($\times 10^{-17}$ erg/s/cm^2)
		Identification				
3770.6	H I	11–2	108 772.34		3769.9	2.5 ± 0.4
3797.9	H I	10–2	108 581.99		3797.2	7.1 ± 0.3
3835.3	H I	9–2	108 324.73		3834.9	9.0 ± 0.4
3889.0	H I	8–2	107 965.06		3888.2	10.5 ± 0.3
3933.7	Ca II	$^2P_{3/2}$–$^2S_{1/2}$	25 414.40		3933.2	28.2 ± 0.3
3968.5	Ca II^a	$^2P_{1/2}$–$^2S_{1/2}$	25 191.51		3968.1	27.6 ± 0.2
3970.1	H I^a	7–2	107 440.45			
4068.6	[SII]	$^2P_{3/2}$–$^4S_{3/2}$	24 571.54		4068.1	98.2 ± 0.2
4076.3	[SII]	$^2P_{1/2}$–$^4S_{3/2}$	24 524.83		4075.9	27.8 ± 0.2
4101.7	H I	6–2	106 632.17		4101.0	15.6 ± 0.2
4114.5	[Fe II]	$b^2H_{11/2}$–$a^4F_{9/2}$	26 170.18		4114.0	1.0 ± 0.4
4244.0	[Fe II]	$a^4G_{11/2}$–$a^4F_{9/2}$	25 428.78		4243.4	3.1 ± 0.2
4276.8	[Fe II]	$a^4G_{9/2}$–$a^4F_{7/2}$	25 805.33		4276.3	1.7 ± 0.2
4319.6	[Fe II]	$a^4G_{7/2}$–$a^4F_{5/2}$	25 981.63		4319.1	1.3 ± 0.2
4340.5	H I	5 –2	105 291.66		4339.7	25.0 ± 0.2
4346.9	[Fe II]	$a^4G_{11/2}$–$a^4F_{7/2}$	25 428.78		4346.1	1.0 ± 0.2
4352.8	[Fe II]	$a^4G_{9/2}$–$a^4F_{5/2}$	25 805.33		4351.5	1.9 ± 0.2
4359.3	[Fe II]	$a^6S_{5/2}$–$a^6D_{7/2}$	23 317.63		4358.6	2.7 ± 0.2
4413.8	[Fe II]	$a^6S_{5/2}$–$a^6D_{5/2}$	23 317.63		4413.3	2.2 ± 0.2
4416.3	[Fe II]	$b^4F_{9/2}$–$a^6D_{9/2}$	22 637.21		4415.7	3.0 ± 0.2
4452.1	[Fe II]	$a^6S_{5/2}$–$a^6D_{3/2}$	23 317.63		4451.4	1.0 ± 0.2
4457.9	[Fe II]	$b^4F_{7/2}$–$a^6D_{7/2}$	22 810.36		4457.4	1.4 ± 0.2
4571.1	Mg I]	$^3P_1$–$^1S_0$	21 870.46		4570.6	6.4 ± 0.2
4728.1	[Fe II]	$b^4P_{3/2}$–$a^6D_{5/2}$	21 812.06		4727.5	1.2 ± 0.1
4814.5	[Fe II]	$b^4F_{9/2}$–$a^4F_{9/2}$	22 637.21		4814.0	2.0 ± 0.1
4861.3	H I	4–2	102 823.90		4860.6	60.4 ± 0.2
4889.6^a	[Fe II]	$b^4P_{5/2}$–$a^6D_{7/2}$	20 830.58		4888.9	1.6 ± 0.1
4889.7^a	[Fe II]	$a^2D_{3/2}$–$a^6D_{3/2}$	21 308.0			
4905.3	[Fe II]	$b^4F_{7/2}$–$a^4F_{7/2}$	22 810.36		4905.0	1.3 ± 0.1
5015.7	He I	$^1P_1$–$^1S_0$	186 209.47		5015.1	5.8 ± 0.2
5111.6	[Fe II]	$a^4H_{11/2}$–$a^4F_{9/2}$	21 430.36		5110.9	1.7 ± 0.2
5158.8	[Fe II]	$a^4H_{13/2}$–$a^4F_{9/2}$	21 251.61		5158.0	6.5 ± 0.2
5197.9	[N I]	$^2D_{3/2}$–$^4S_{3/2}$	19 233.18		5197.5	6.1 ± 0.2
5200.2	[N I]	$^2D_{5/2}$–$^4S_{3/2}$	19 224.46		5199.8	3.4 ± 0.2
5220.1	[Fe II]	$a^4H_{9/2}$–$a^4F_{7/2}$	21 581.64		5219.5	1.4 ± 0.2
5261.6	[Fe II]	$a^4H_{11/2}$–$a^4F_{7/2}$	21 430.36		5260.9	3.6 ± 0.2
5273.3	[Fe II]	$b^4P_{5/2}$–$a^4F_{9/2}$	20 830.58		5272.7	1.5 ± 0.2
5333.6	[Fe II]	$a^4H_{9/2}$–$a^4F_{5/2}$	21 581.64		5333.0	2.8 ± 0.2
5376.5	[Fe II]	$a^4H_{7/2}$–$a^4F_{3/2}$	21 711.92		5375.8	2.4 ± 0.2
5412.7	[Fe II]	$a^2D_{3/2}$–$a^4F_{5/2}$	21 308.04		5411.9	0.8 ± 0.2
5527.3^a	[Fe II]	$a^2D_{5/2}$–$a^4F_{7/2}$	20 516.96		5526.7	3.3 ± 0.2
5527.6^a	[Fe II]	$b^2P_{1/2}$–$a^4D_{1/2}$	26 932.75			
5577.3	[O I]	$^1S_0$–$^1S_2$	33 792.58		5576.7	11.6 ± 0.3
5875.9	He I	$^3D_1$–$^3P_0$	186 101.7		5875.3	8.2 ± 0.2
5890.1	Cr II]	$^6D_{3/2}$–$v^4F_{5/2}$	107 414.7		5889.2	7.6 ± 0.2
5895.9	Fe I	i^5D_2–x^5F_2	57 974.1		5895.2	5.3 ± 0.2
6300.3	[O I]	$^1D_1$–$^3P_2$	15 867.9		6299.7	248.3 ± 0.3
				B	6299.5	54.4 ± 0.3
				R	6299.8	63.6 ± 0.3
6363.7	[O I]	$^1D_2$–$^3P_1$	15 867.9		6363.1	81.8 ± 0.3
				B	6362.8	16.4 ± 0.3
				R	6363.1	19.2 ± 0.3
6548.0	[N II]	$^1D_2$–$^3P_1$	15 316.2		6547.7	4.7 ± 0.2
6562.8	H I	3–2	97 492.31		6562.4	841.4 ± 0.2
6583.5	[N II]	$^1D_2$–$^3P_2$	15 316.2		6583.0	10.5 ± 0.2
				B	6583.3	3.8 ± 0.2
				R	6582.6	3.5 ± 0.2

Notes. Fluxes refer to the source spectrum (extracted over the range –0.5 ″to 0.5 ″), are in units of erg/s/cm^2 × 10^{-17} and are not extinction corrected. Where the identified lines are also found in the extended blue (B) and red-shifted (R) jets the observed wavelengths and fluxes are also given. The spatial regions corresponding to B and R are marked in Fig. 7. The horizontal lines separate the UVB, VIS and NIR arms. $^{(a)}$ blended lines.

Table A.2. continued.

λ_{air} (Å)	Identification Ion	Type	E_u (cm^{-1})	Jet	λ_{obs} (Å)	Flux ($\times 10^{-17}$ erg/s/cm^2)
6678.2	He I	$^1D_2$–$^1P_1$	186 105.1		6677.7	3.6 ± 0.2
6716.4	[S II]	$^2D_{5/2}$–$^4S_{3/2}$	14 884.7		6716.0	29.6 ± 0.2
				B	6715.6	10.1 ± 0.2
				R	6716.4	14.1 ± 0.2
6730.8	[S II]	$^2D_{3/2}$–$^4S_{3/2}$	14 852.9		6730.4	56.3 ± 0.2
				B	6729.9	15.1 ± 0.2
				R	6730.8	22.7 ± 0.2
7065.7	He I	$^3S_1$–$^3P_0$	183 236.9		7064.8	2.6 ± 0.3
7155.2	[Fe II]	$a^2G_{9/2}$–$a^4F_{9/2}$	15 844.7		7154.5	9.5 ± 0.1
7172.0	[Fe II]	$a^2G_{7/2}$–$a^4F_{7/2}$	16 369.4		7171.3	2.9 ± 0.1
7291.4	[Ca II]	$^2D_{5/2}$–$^2S_{1/2}$	13 710.9		7291.1	2.1 ± 0.2
7319.9	[O II]	$^2P_{5/2}$–$^2D_{3/2}$	40 468.01		7319.2	2.9 ± 0.2
7330.7	[O II]	$^2P_{3/2}$–$^2D_{3/2}$	40 468.01		7329.7	1.7 ± 0.2
7377.8	[Ni II]	$^2F_{7/2}$–$^2D_{5/2}$	13 550.4		7377.2	3.4 ± 0.2
7388.2	[Fe II]	$a^2G_{7/2}$–$a^4F_{5/2}$	16 369.4		7387.6	3.1 ± 0.2
7411.6	[Ni II]	$^2F_{5/2}$–$^2D_{3/2}$	14 955.0		7412.1	0.9 ± 0.2
7452.5	[Fe II]	$a^2G_{9/2}$–$a^4F_{7/2}$	15 844.7		7451.8	3.3 ± 0.2
8498.0	Ca II	$^2P_{3/2}$–$^2D_{3/2}$	25 414.4		8497.3	36.8 ± 0.2
8542.1	Ca II	$^2P_{3/2}$–$^2D_{5/2}$	25 414.4		8541.2	39.6 ± 0.2
8617.0	[Fe II]	$a^4P_{5/2}$–$a^4F_{9/2}$	13 474.4		8616.1	6.8 ± 0.3
8662.1	Ca II	$^2P_{1/2}$–$^2D_{3/2}$	25 191.5		8661.3	35.5 ± 0.2
8727.1	[C I]	$^1S_0$–$^1D_2$	21 648.0		8726.6	36.1 ± 0.2
8891.9	[Fe II]	$a^4P_{3/2}$–$a^4F_{7/2}$	2430.1		8891.2	2.9 ± 0.8
9226.6[a]	[Fe II]	$a^4P_{3/2}$–$a^4F_{3/2}$	13 673.2		9227.4	20.8 ± 0.8
9227.8[a]	He I	^3P–^3D	196 935.4			
9850.3	[C I]	$^1D_2$–$^3P_2$	10 192.6		9849.6	85.4 ± 0.2
10 286.7	[S II]	$^2P_{3/2}$–$^2D_{3/2}$	24 571.5		10 285.4	38.8 ± 0.6
10 320.5	[S II]	$^2P_{3/2}$–$^2D_{5/2}$	24 571.5		10 319.2	48.3 ± 0.6
10 336.4	[S II]	$^2P_{1/2}$–$^2D_{3/2}$	24 524.8		10 335.1	30.2 ± 0.6
10 370.5	[S II]	$^2P_{1/2}$–$^2D_{5/2}$	24 524.8		10 369.3	14.6 ± 0.6
10 397.7[a]	[N I]	$^2P_{3/2}$–$^2D_{5/2}$	28 839.3		10 396.5	40.0 ± 0.6
10 398.2[a]	[N I]	$^2P_{1/2}$–$^2D_{5/2}$	28 839.9			
10 407.2[a]	[N I]	$^2P_{3/2}$–$^2D_{3/2}$	28 839.3		10 406.1	31.2 ± 0.6
10 407.6[a]	[N I]	$^2P_{1/2}$–$^2D_{3/2}$	28 838.9			
10 830.3	He I	$^3P_1$–$^3S_1$	169 087.0		10 828.0	78.0 ± 0.6
10 938.0	H I	6–3	106 632.2		10 936.3	44.2 ± 0.6
12 566.8	[Fe II]	$a^4D_{7/2}$–$a^6D_{9/2}$	7955.3		12 565.6	13.1 ± 0.7
12 787.8	[Fe II]	$a^4D_{3/2}$–$a^6D_{3/2}$	8680.5		12 786.1	3.7 ± 0.7
12 818.1	H I	5–3	105 291.7		12 815.5	73.8 ± 0.7
12 942.7	[Fe II]	$a^4D_{5/2}$–$a^6D_{5/2}$	8391.9		12 941.4	3.4 ± 0.7
16 435.5	[Fe II]	$a^4D_{7/2}$–$a^4F_{9/2}$	7955.3		16 433.3	11.2 ± 0.8
21 212.5	H$_2$	1-0S(1)			21 210.0	11.6 ± 0.8
21 655.3	H I	7–4	107 440.5		21 650.4	16.4 ± 0.6